GEOTECHNICAL ENGINEERING

LUNAR SURFACE ENGINEERING PROPERTIES EXPERIMENT DEFINITION

FINAL REPORT: VOLUME II OF IV
LUNAR SOIL PROPERTIES FROM PHOTOGRAPHIC RECORDS

by

JAMES K. MITCHELL

PREPARED FOR MARSHALL SPACE FLIGHT CENTER
HUNTSVILLE, ALABAMA UNDER NASA CONTRACT
NAS 8-21432

JANUARY, 1970

SPACE SCIENCES LABORATORY

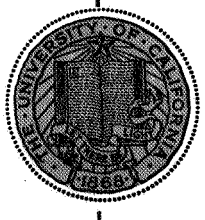

UNIVERSITY OF CALIFORNIA · BERKELEY

University of California
Berkeley
Geotechnical Engineering

LUNAR SURFACE ENGINEERING PROPERTIES EXPERIMENT DEFINITION

FINAL REPORT: VOLUME II OF IV
LUNAR SOIL PROPERTIES FROM PHOTOGRAPHIC RECORDS

by

James K. Mitchell

Contract Number NAS 8-21432

Control Number DCN 1-8-28-00056(IF)

January, 1970

Submitted to
National Aeronautics and Space Administration
George C. Marshall Space Flight Center

Space Sciences Laboratory Series 11, Issue 11

This report was prepared by the University of California, Berkeley, under Contract Number NAS 8-21432, Lunar Surface Engineering Properties Experiment Definition for the George C. Marshall Space Flight Center of the National Aeronautics and Space Administration. The work was administered under the technical direction of the Space Sciences Laboratory of the George C. Marshall Space Flight Center.

PREFACE

This report presents the results of studies conducted during the period June 20, 1968 - July 19, 1969, under NASA research contract NAS 8-21432, "Lunar Surface Engineering Properties Experiment Definition." This study was sponsored by the Advanced Lunar Missions Directorate, NASA Headquarters, and was under the technical cognizance of Dr. N. C. Costes, Space Science Laboratory, George C. Marshall Space Flight Center.

The report reflects the combined effort of four faculty investigators, a research engineer, a project manager, and six graduate research assistants, representing several engineering and scientific disciplines pertinent to the study of lunar surface material properties. James K. Mitchell, Professor of Civil Engineering, served as Principal Investigator and was responsible for those phases of the work concerned with problems relating to the engineering properites of lunar soils and lunar soil mechanics. Co-investigators were William N. Houston, Assistant Professor of Civil Engineering, who was concerned with problems relating to the engineering properties of lunar soils; Richard E. Goodman, Associate Professor of Geological Engineering, who was concerned with the engineering geology and rock mechanics aspects of the lunar surface; and Paul A. Witherspoon, Professor of Geological Engineering, who conducted studies related to thermal and permeability measurements on the lunar surface. Dr. Karel Drozd, Assistant Research Engineer, performed laboratory tests and analyses pertinent to the development of a borehole probe for determination of the in-situ characteristics of lunar soils and rocks. John Hovland, David Katz, Laith I. Namiq, James B. Thompson, Tran K. Van, and Ted S. Vinson served as Graduate Research Assistants and carried out many of the studies leading to the results presented in this report. Francois Heuzé, Assistant Specialist, served as project manager and contributed to studies concerned with lunar rock mechanics.

Ultimate objectives of this project are:

1) Assessment of lunar soil and rock property data using information obtained from Lunar Orbiter and Surveyor missions.
2) Recommendation of both simple and sophisticated in-situ testing techniques that would allow determination of engineering properties of lunar surface materials.
3) Determination of the influence of variations in lunar surface conditions on the performance parameters of a lunar roving vehicle.
4) Development of simple means for determining the fluid and thermal conductivity properties of lunar surface materials.
5) Development of stabilization techniques for use in loose, unconsolidated lunar surface materials to improve the performance of such materials in lunar engineering application.

The scope of specific studies conducted in satisfaction of these objectives is indicated by the following list of contents from the Detailed Final Report which is presented in four volumes. The names of the investigators associated with each phase of the work are indicated.

VOLUME I

MECHANICS AND STABILIZATION OF LUNAR SOILS

VOLUME II

LUNAR SOIL PROPERTIES FROM PHOTOGRAPHIC RECORDS

VOLUME III

BOREHOLE PROBES

VOLUME IV

FLUID CONDUCTIVITY OF LUNAR SURFACE MATERIALS

VOLUME II OF FOUR

CONTENTS

VOLUME II OF FOUR (Cont'd) CONTENTS

CHAPTER 1

SOIL PROPERTY EVALUATIONS FROM BOULDER TRACKS ON THE LUNAR SURFACE

(H. J. Hovland and J. K. Mitchell)

I. INTRODUCTION

Among the conspicuous and interesting features on the lunar surface are large boulders and the tracks they left as they rolled down slopes. These features were observed early on photographs provided by Lunar Orbiters. The tracks appear to be of three different types, i.e., (1) continuous tracks suggestive of a spherical boulder rolling uniformly down the slope, (2) segmented tracks suggestive of bouncing, and (3) relatively short tracks suggestive of plowing. An example of a typical lunar boulder track is shown in Figure 1-1.

It was soon recognized that a relationship must exist between the size of the boulder and the track that it left, and that this relationship would include both soil and boulder properties. Hence, some lunar boulders have been previously studied (Filice, 1967; Nordmeyer and Mason, 1967; Moore and Martin, 1967; Eggleston, et al., 1968). These early investigations were aimed primarily at determining the static bearing capacity of lunar surface soil. Currently we are investigating the possibilities for deducing soil strength parameters (cohesion and angle of internal friction) in more detail.

A summary of the work done by our group on the study of lunar boulder tracks during the year 1967-68 was presented in the final report for Contract NSR 05-003-189 (Mitchell et al., 1969). In this report, several methods for analyzing boulder-track data were considered,

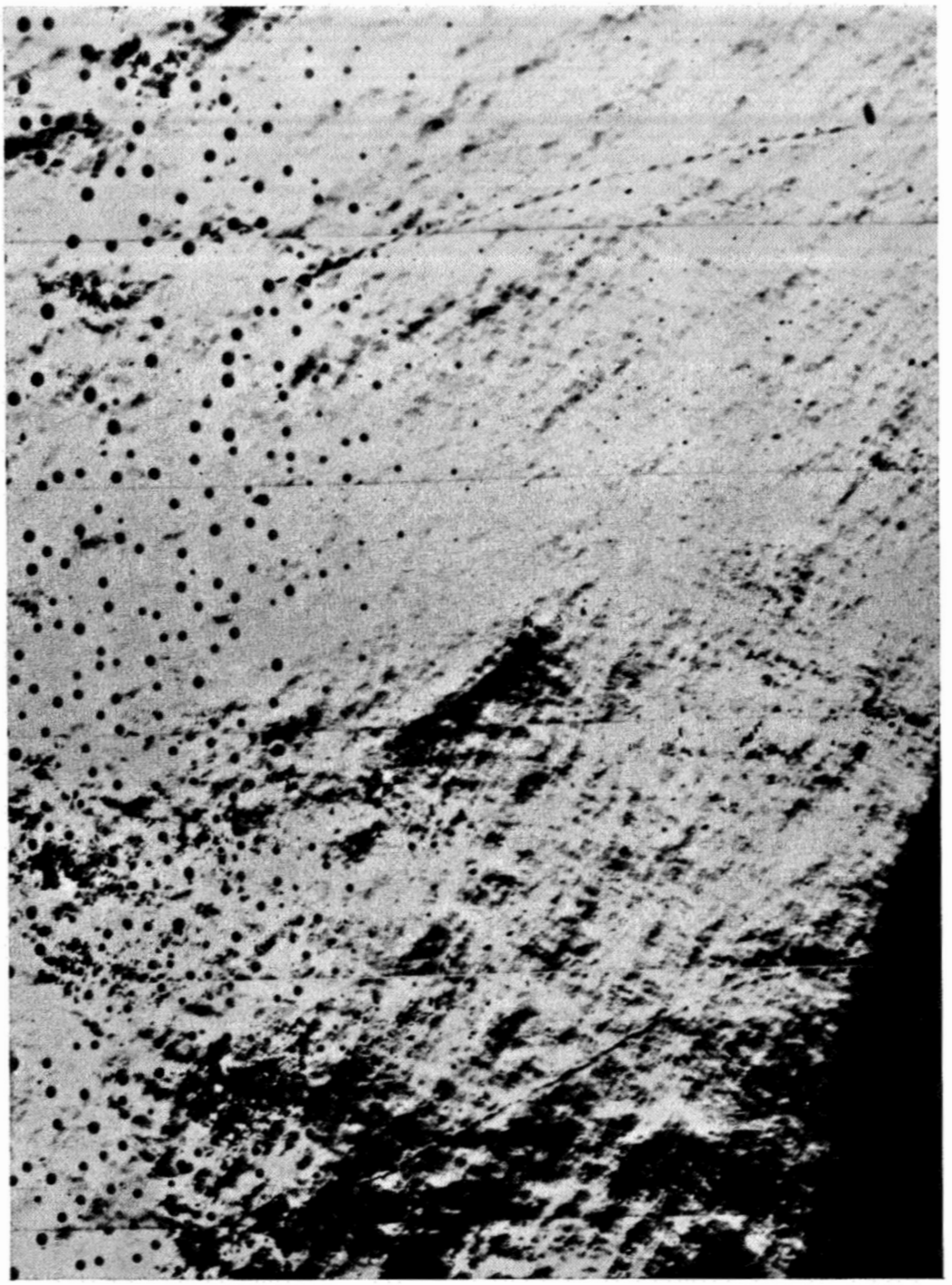

FIGURE 1-1 TYPICAL BOULDER TRACKS

each subject to limitations and giving somewhat different results. It was recommended that boulder track phenomena be further studied, and it was noted also that if variability of the lunar surface is to be determined, it is important to use the same method of analysis throughout.

Studies this year (1968-69) have consisted of further study of Orbiter photography for the purpose of locating suitable boulder tracks for analysis, study of site geology for selected boulder tracks, and static analysis of the boulder tracks using bearing capacity theory. The same method has been applied to 69 boulder tracks from 19 different areas of the moon, as shown on Figure 1-2. These areas include lunar upland, maria, and perhaps intermediate terrain.

This report presents the results of the studies to date. The general nature of the boulder track locations and tentative geology of such locations are first described followed by the analysis. The results suggest a variability of lunar soils; possible causes of such variability are considered.

II. GEOLOGY OF BOULDER TRACK LOCATIONS

Boulder track analysis has been proposed as a method for studying both the variability of lunar soils and for estimating actual soil property values. This section presents possible geological conditions at the boulder track locations studied. This type of information must complement the study of variability of lunar soils from boulder tracks. Also, in the boulder track analysis, the evaluation of the friction angle requires at the present time certain critical assumptions

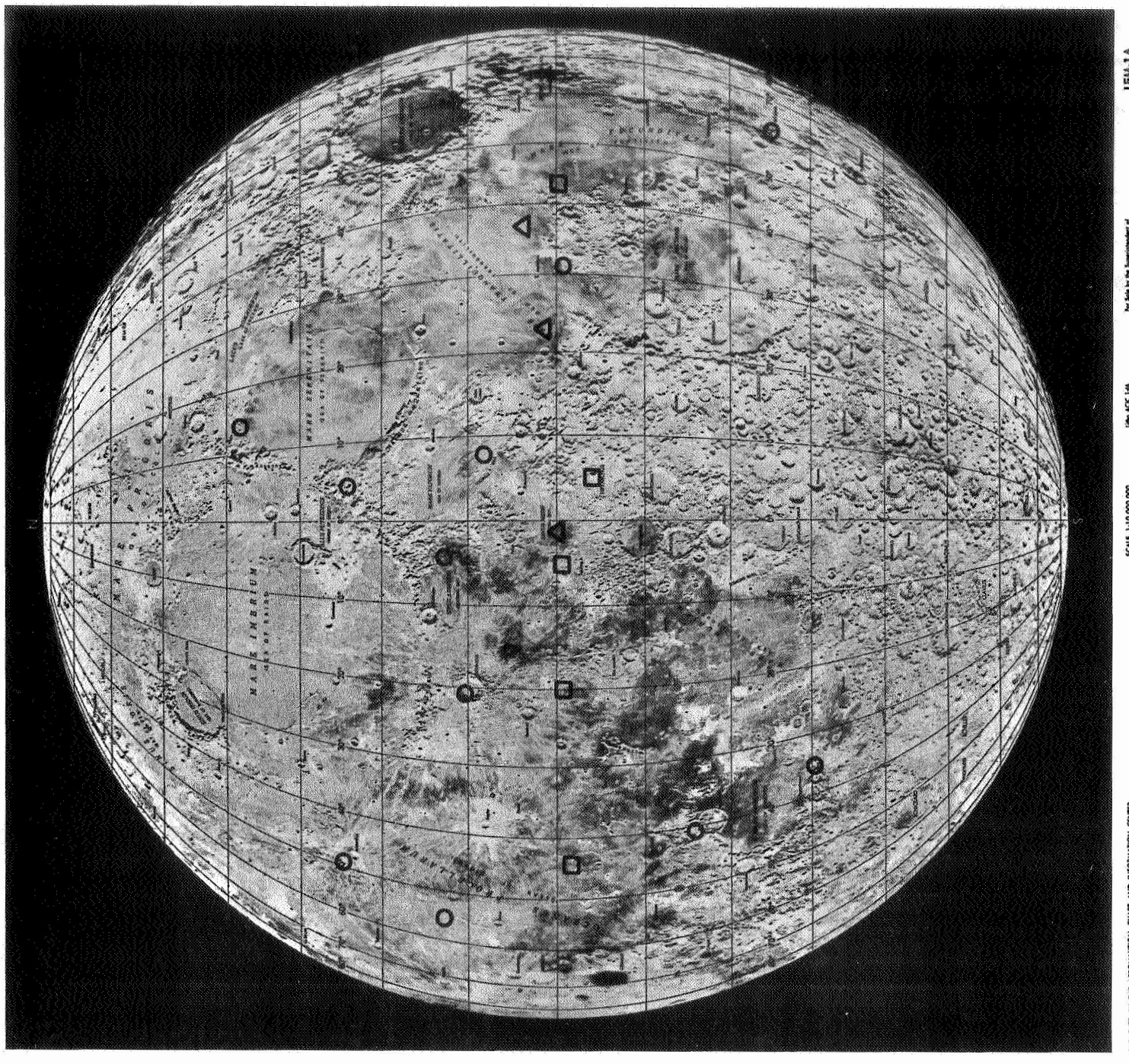

FIGURE 1-2 LOCATIONS OF BOULDER TRACKS ANALYZED

regarding cohesion and density. The type of information presented in this section may make it possible to consider separately for each location assumptions regarding cohesion and density.

Tentative conclusions about the geology of the actual boulder track locations were drawn with the aid of USGS geologic quadrangle maps of the moon (USGS 1963-1968), USGS "Generalized Photogeologic Map of the Moon" (Hackman, 1961) where quadrangle maps were not available, and high resolution Lunar Orbiter photographs. Surveyor results and literature on the subject were also consulted (Surveyor Mission Reports, Langley Working Paper 506, 1968). The results of this study are presented in Table 1-1. The USGS symbols in this table are as found on the maps and represent geologic formations mapped primarily on physiographic evidence, i.e., the formation overlying or intruding another, or having a lower crater density, is considered younger. General definition of the USGS symbols used is presented in Table 1-2 (USGS maps). A relative chronology of lunar geological events is presented in Table 1-3 (USGS maps). The interpretation in Table 1-1 is partly based on the maps and literature and partly on the writers' study of the orbiter photographs. East longitudes and north latitudes are positive.

Based on the information presented in Table 1-1, the following generalizations can be made relative to the geology and surface materials in the areas of boulder tracks:

1. Volcanic materials predominate.
2. Materials of possibly higher porosity and lower density, such as volcanic ash and sometimes lunar ray materials, are quite common.

TABLE 1-1

Geology of Boulder Track Locations

Location	Frame	Longitude (degrees)	Latitude (degrees)	USGS Map No.	Material	
					USGS* Symbols	Interpretation
Mare Tranquillitatis (Approx. 100 Km from Apollo Site)	Orbiter II 27H	36.54	3.56	I-351	M**	Probably mare material composed of volcanic flows and fragmental material
Sabine D (Approx. 30 Km from Surveyor 5 and Apollo Site 2)	76H	23.68	1.20	I-510	Imp2 + ray + Csc	Ray material over Imbrian volcanics. Possibly also some satellitic crater material
Sinus Medii (Approx. 20 Km from Surveyor 6 and Apollo site 3)	122H	-1.32	0.32	I-548	Ipm1	Imbrian volcanics, probably lava and ash flows and some pyroclastics (mare material)
Sinus Medii (Approx. 20 Km from Surveyor 6 and Apollo Site 3)	123H	-1.89	0.29	I-548	Ipm1	Imbrian volcanics, probably lava and ash flows and some pyroclastics (mare material)
	Orbiter III					
Mare Fecunditatis (Approx. 150 Km WNW of Messier A)	35H	42.81	-1.05	I-351	pM**	Post-maria rocks consisting likely of maria crater colluvium
NE Mosting	107H	-5.67	-0.33	I-566	Cs+Ccw	Copernican slope and crater wall materials (fresh colluvium)
Rima Hipparcus	111H	4.83	-4.92	I-566	Ica	Crater colluvium composed probably of volcanic ash and other fragmental material

*Symbols used on USGS Quadrangle maps of the moon to designate formations (see page 1-65).

**R. J. Hackman, "Generalized Photogeologic Map of the Moon", Map I-351, Sheet 1 of 4, USGS, 1961.

Table 1-1 Cont'd

Location	Frame	Longitude (degrees)	Latitude (degrees)	USGS Map No.	Material	
					USGS* Symbols	Interpretation
Reinhold (Approx. 30 Km East of Reinhold K)	125H	-20.02	-0.60	I-458	Imp	Imbrian volcanic flows, probably thick flows of basalt or ignimbrite w/some ray and fragmental material
Oceanus Procellarum (Approx. 40 Km from Surveyor 1)	181H	-43.54	-2.11	I-385	Pm+ray	Probably thick flows of basalt or ignimbrite with some ray material
Oceanus Procellarum (Approx. 40 Km from Surveyor 1	189H	-44.17	-2.41	I-385	Pm+ray	Ray material and fragmental crater rim material over Procellarian volcanic flows (Pm - same as above)
	Orbiter V					
Central mountains of Petavius (Rille)	34H	60.57	-25.70	I-351	aM**	Premaria rocks (undivided), fragmental accretionary talus material
Mare Tranquillitatis	63H	32.75	-0.44	I 351	aM,M**	Likely both maria and premaria rocks consisting of fragmental accretionary and volcanic flow material
Large Hill South of Alexander	88H	13.54	38.92	I-351	aM,pM**	Likely both maria and postmaria rocks (volcanics, crater and ray materials)
SE part of Hyginus	95H	5.94	7.56	I-548	Ipm?, Cs ch, chf	Fresh talus and colluvium composed of crater rim, wall, and related volcanic material with some mare volcanic material.
NE part of Hyginus	96H	5.96	7.85	I-548	Cs, chf	Fresh talus and colluvium composed of crater rim, wall and related volcanic material

Table 1-1 Cont'd

Location	Frame	Longitude (degrees)	Latitude (degrees)	USGS Map No.	Material	
					USGS* Symbols	Interpretation
NE part of Hyginus	97H	5.98	8.14	I-548	ch, Ica	Crater related volcanic material and mare material with impact debris
Hadley Rille	105H	2.95	25.00	I-463	sr	Sinuous rille material consisting of volcanic ash, lava, and talus
Rima Bode	122H	-3.97	12.92	I-548	Cs, ir	Talus and colluvium consisting probably mostly of volcanic material
Copernicus (center)	151H	-20.34	9.42	I-515	Ccfh	Copernican shock crushed breccia
Copernicus (NW of center)	155H	-20.24	10.58	I-515	Ccw	Copernican dark rim material and slumped talus
Copernicus (NW of center)	156H	-20.21	10.87	I-515	Ccw+Cs	Rim material and fresh talus
Center of Vitello	168H	-37.57	-30.61	I-495	Iplgf	Gassendi Group, eroded crater
Rima Bode	122H	-3.97	12.92	I-548	Cs, ir	Talus and colluvium consisting probably mostly of volvanic material
Copernicus (center)	151H	-20.34	9.42	I-515	Ccfh	Copernican shock crushed breccia
Copernicus (NW of center)	155H	-20.24	10.58	I-515	Ccw	Copernican dark rim material and slumped talus
Copernicus (NW of center)	156H	-20.21	10.87	I-515	Ccw+Cs	Rim material and fresh talus
Center of Vitello	168H	-37.57	-30.61	I-495	Iplgf	Gassendi group, eroded crater material covered partly with mare material
Gassendi (NW rim)	179H	-39.97	-16.29	I-495	Ccr	Talus and probably poorly sorted ejecta of impact origin

TABLE 1-1 Cont'd

Location	Frame	Longitude (degrees)	Latitude (degrees	USGS Map No.	Material	
					USGS* Symbols	Interpretation
Schröter's Valley	203H	-49.51	25.13	I-465	Cs,Csr,CEv	Talus and colluvium probably consisting of volcanic ash and flow material
Schröter's Valley	204H	-49.48	25.52	I-465	Cs,Csr,CEv	Talus and colluvium probably consisting of volcanic ash and flow material
Oceanus Procellarum (Approx. 130 Km NW of Marius)	213H	-56.03	13.50	I-491	sr?, Eml	Talus and colluvium probably consisting of volcanic flow and pyroclastic materials

TABLE 1-2

Definition of USGS Symbols

Symbol	Definition
	Symbols used on the Geologic Quadrangle Maps of the Moon
	Copernican System
Cs	Slope material
Ccfh	Crater floor material, hummocky
Ccr	Crater rim material
Ccw	Crater wall material
Csc	Satellitic crater material
CEv	Vallis Schröteri Formation
Ch	Cobra Head Formation (Ejecta-flow blanket)
Csr	Sinuous rille material
	Eratosthenian System
Eml	Marius Group, smooth undulating material
	Procellarian System
Pm	Mare material
	Imbrian System
Ipm	Procellarum Group, mare material, relatively low albedo
Ipm 1	Procellarum Group, mare material, higher albedo
Ipm 2	Procellarum Group, mare material, intermediate albedo
Ica	Cayley Formation
	Pre-Imbrian
	Gassendi group, floor material
	Unit not assigned ages
ir	Irregular ring material
sr	Sinuous rille
ch	Chain crater material, rim and wall
chf	Chain crater material, floor
	Symbols used on the "Generalized Photogeologic Map of the Moon,"*
pM	Post-maria rocks (undivided)
M	Maria rocks (undivided)
aM	Pre-maria rocks (undivided)

*R. J. Hackman, "Generalized Photogeologic Map of the Moon", Map I-351, Sheet 1 of 4, USGS, 1961.

TABLE 1-3

Relative Chronology of Lunar Geological Events

Period	Epoch	Events
Copernican		Formation of rayed craters
Eratosthenian		Formation of craters whose rays are no longer visible
Imbrian	Archimedian	Deposition of mare materials of the Procellarum Group. Formation of craters older than at least part of the Procellarum Group
	Apenninian	Events related to the formation of the mare Imbrium basin
Pre-Imbrium		No yet formally divided

3. Boulders rolled over talus or colluvium, consequently, considerable mixing of parent materials would be expected.
4. The material identification is too vague to serve as a basis for specific quantitative conclusions.

III. THEORY FOR BOULDER TRACK ANALYSIS

A. Geometrical Relations of Sphere and Track

A boulder rolling on a slope where the soil fails in general shear would leave a track with a raised rim, as shown on Figure 1-3. Raised rims have been observed on many lunar boulder tracks. For the purpose of the present analysis, the theory will be developed for a somewhat more idealized situation, assuming a sphere as shown on Figure 1-4.

From Figure 1-4 it may be seen that the track depth will be given by

$$z = r(1 - \cos\theta) = r\ (1 - \cos[\sin^{-1}\frac{w}{D}]) \qquad (1\text{-}1)$$

where $D = 2r$, or the sphere diameter.

The semicircular soil-sphere contact area may be represented by an equivalent rectangular area defined by

$$2b^2 = \frac{w^2}{4}\frac{\pi}{2}\ , \text{ giving} \qquad (1\text{-}2)$$

$$b = \frac{w}{4}\sqrt{\pi} = 0.44\ w. \qquad (1\text{-}3)$$

If $\alpha = 0$, i.e.,a horizontal surface, the resultant force that would cause the sphere to move and a track to form must be inclined at some angle to the direction of the weight of the sphere. Assuming that this resultant goes through the centroid of the soil-sphere contact area, the maximum value of this resultant would be approximately $\sqrt{2}$ times the

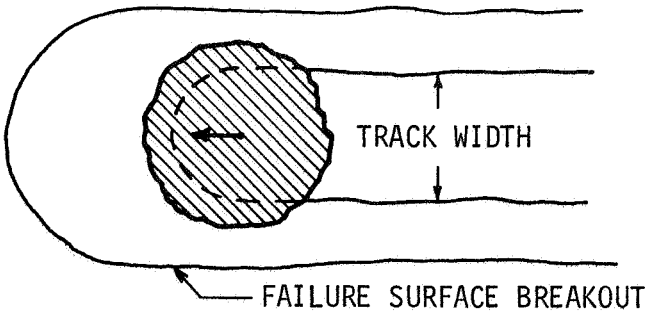

TOP VIEW

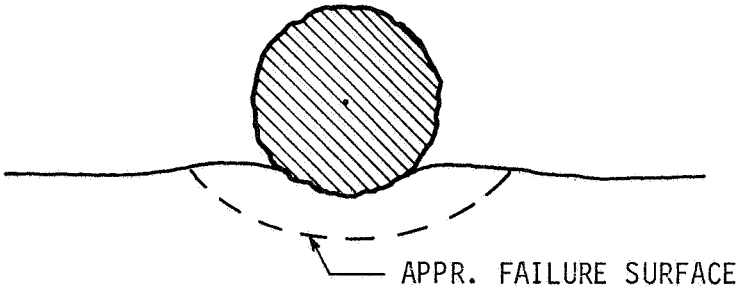

FRONT VIEW

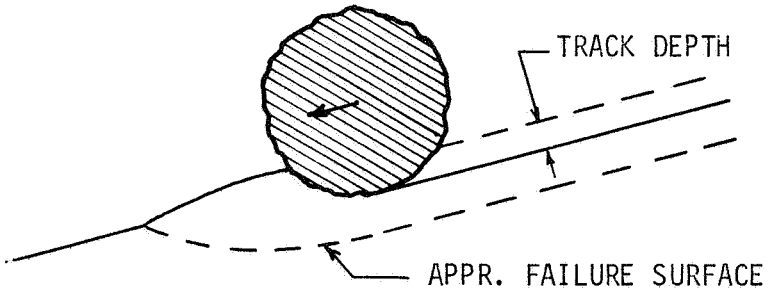

SIDE VIEW

FIGURE 1-3 BOULDER ROLLING DOWN SLOPE

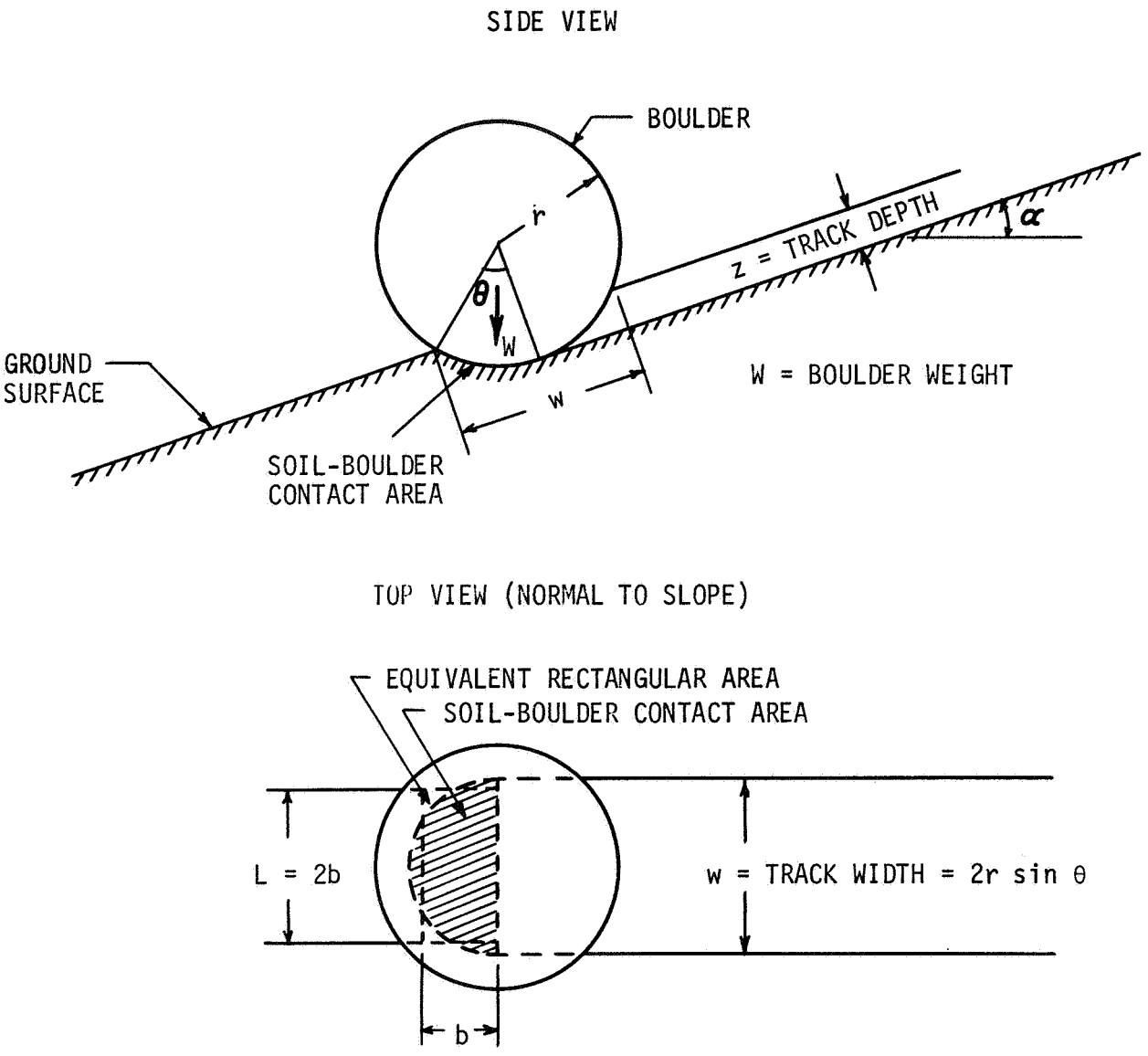

FIGURE 1-4 GEOMETRICAL RELATIONS OF SPHERE AND TRACK

weight of the sphere and would occur when the ratio of w/D = 1. This is because for w/D = 1 sinkage is maximum, soil-sphere contact area is maximum, and the centroid at the soil-sphere contact area is furthest from the point vertically below the sphere. For smaller ratios of w/D or slope angles greater than zero, the magnitude of the resultant would be more nearly equal to the weight at the sphere. It will therefore be assumed in the following static analysis that the magnitude of the resultant force equals the weight of the sphere. In actuality, the horizontal component of the resultant would depend on the velocity of the sphere.

B. Modified Bearing Capacity Theory

A general bearing capacity equation for a strip footing is (Leonards, 1962)

$$q = \frac{\gamma b}{2} N_\gamma + cN_c + q' N_q \qquad (1\text{-}4)$$

For a rectangular footing this equation may be modified to

$$q = \frac{\gamma b}{2} N_\gamma s_\gamma + cN_c s_c + q' N_q s_q \qquad (1\text{-}5)$$

In these equations

q = unit bearing capacity

γ = unit weight of soil

b = width of footing

c = soil cohesion

q' = surcharge

s_γ, s_c, s_q = shape factors, and

N_γ, N_c, N_q = bearing capacity factors which depend on the soil friction angle, ϕ.

Skempton (1951) indicated that for $\phi = 0$, the value of s_c can be taken as (1 + 0.2 b/L), where L is the length of a rectangular footing. For $\phi > 0$, the value of s_c would probably not be significantly different. Meyerhof (1951) proposed that for $\phi = 30°$, s_q equals approximately (1 + 0.2 b/L). The friction angle for lunar soil is likely close enough to 30° to justify the use of this value for s_q. The shape factor, s_γ, is given by (1 - 0.3 b/L) according to Lundgren and Hansen (1955) and Hansen (1957).

Substituting these shape factors into the bearing capacity equation we get

$$q = \frac{\gamma b}{2}\left(1 - 0.3\,\frac{b}{L}\right)N_\gamma + c\left(1 + 0.2\,\frac{b}{L}\right)N_c + q'\left(1 + 0.2\,\frac{b}{L}\right)N_q. \qquad (1\text{-}6)$$

for the sphere b/L = 1/2 and b = 0.444 w. If also an average surcharge depth is taken to be z/2,

$$q = \frac{0.85}{2}(0.444\,w)\gamma N_\gamma + 1.1\,cN_c + \frac{1.1}{2}\,\gamma z N_q. \qquad (1\text{-}7)$$

A convenient equation in dimensionless form results by dividing both sides by $(w\gamma)$ to give

$$\frac{q}{w\gamma} = 0.188\,N_\gamma + 1.1\left(\frac{c}{w\gamma}\right)N_c + 0.55\left(\frac{z}{w}\right)N_q. \qquad (1\text{-}8)$$

Defining q_e as the unit bearing capacity in earth gravity and γ_e as the unit weight of soil in earth gravity, the equation for the unit bearing capacity of a sphere in the earth gravity field becomes

$$\frac{q_e}{w\gamma_e} = 0.188\,N_\gamma + 1.1\left(\frac{c}{w\gamma_e}\right)N_c + 0.55\left(\frac{z}{w}\right)N_q. \qquad (1\text{-}9)$$

This equation is readily adopted for estimation of the bearing capacity on the moon by noting that for a given soil mass density, the unit weight on the moon will be reduced by a factor of six. Thus, if q_m designates the bearing capacity on the moon, Equation (1-9) becomes

$$\frac{q_m}{w\gamma_e} = 0.0314\ N_\gamma + 1.1\left(\frac{c}{w\gamma_e}\right)N_c + 0.0916\ \left(\frac{z}{w}\right)\ N_q \qquad (1\text{-}10)$$

The influence of the slope angle, α, can be incorporated by using Meyerhof's bearing capacity factors (Meyerhof 1951). For the purpose of this study, the charts for Meyerhof's bearing capacity factors were enlarged and are presented on Figures 1-5, 1-6, and 1-7.

Graphs have also been prepared for Equation (1-10), as shown in Figures 1-8 through 1-15 to give $(q_m/\gamma_e w)$ vs. $(c/\gamma_e w)$ for different values of ϕ, z/w, and slope angle, α. Separate charts are shown for z/w = 0 and z/w = 0.5 and slope angles of 0, 10, 20, and 30 degrees. These ranges of parameters probably cover most cases that are likely to be encountered in practice. Linear interpolation is valid for cases between no sinkage (z/w = 0) and sinkage equal to the radius of the sphere (z/w = 0.5). Although straight line interpolation is not strictly valid for slope angles, the error from such interpolation is small.

A second expression for the bearing capacity of a sphere can be developed from the ratio of sphere weight to bearing area. This gives

$$q = \frac{4/3\pi r^3\gamma_r}{\frac{\pi}{2}\frac{w^2}{4}} = \frac{32}{3}\ \frac{r^3}{w^2}\gamma_r = \frac{4}{3}\ \frac{D\gamma_r}{(w/D)^2}, \qquad (1\text{-}11)$$

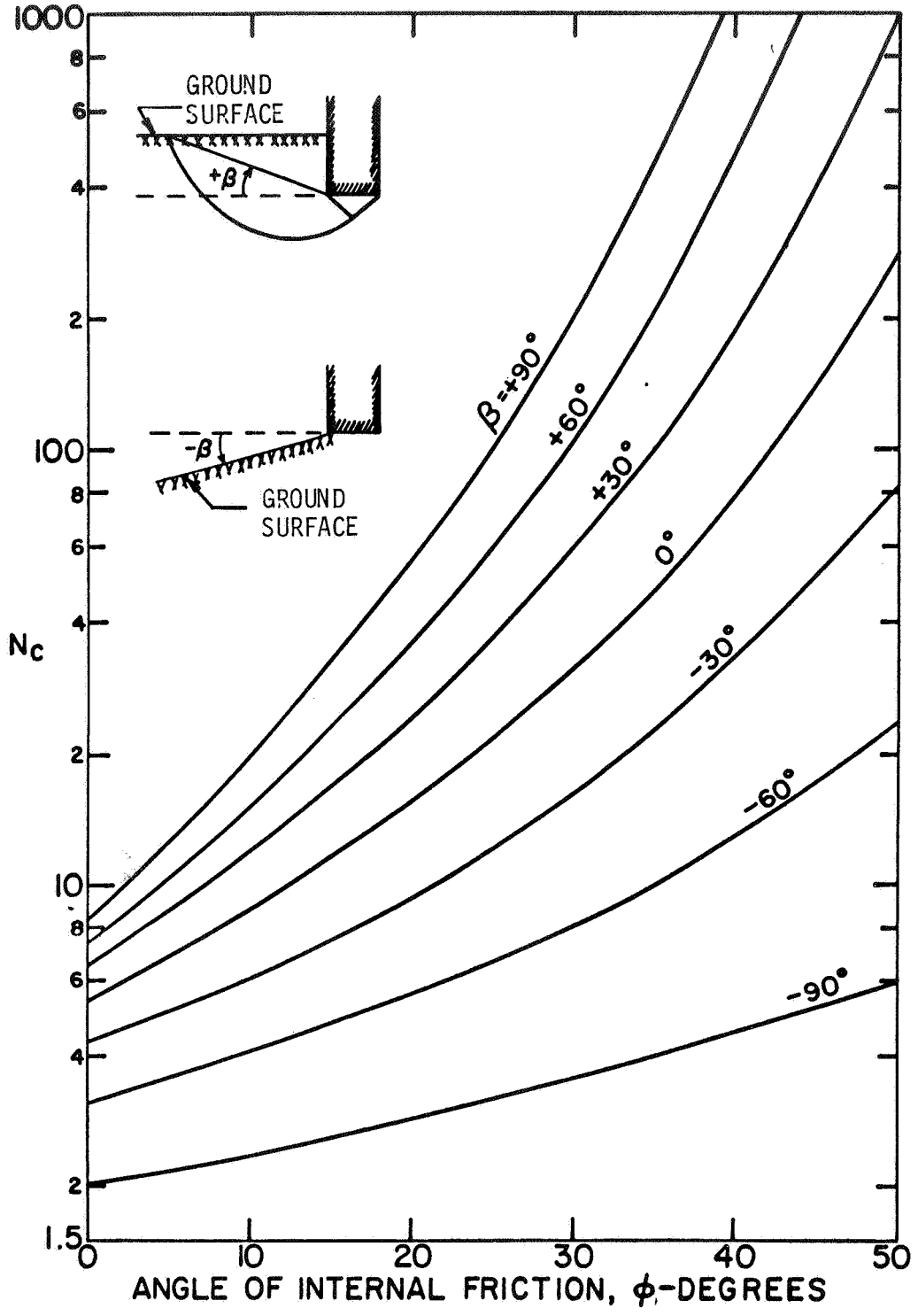

FIGURE 1-5 GENERAL BEARING CAPACITY FACTOR N_c FOR STRIP FOUNDATION (After Meyerhoff, 1951)

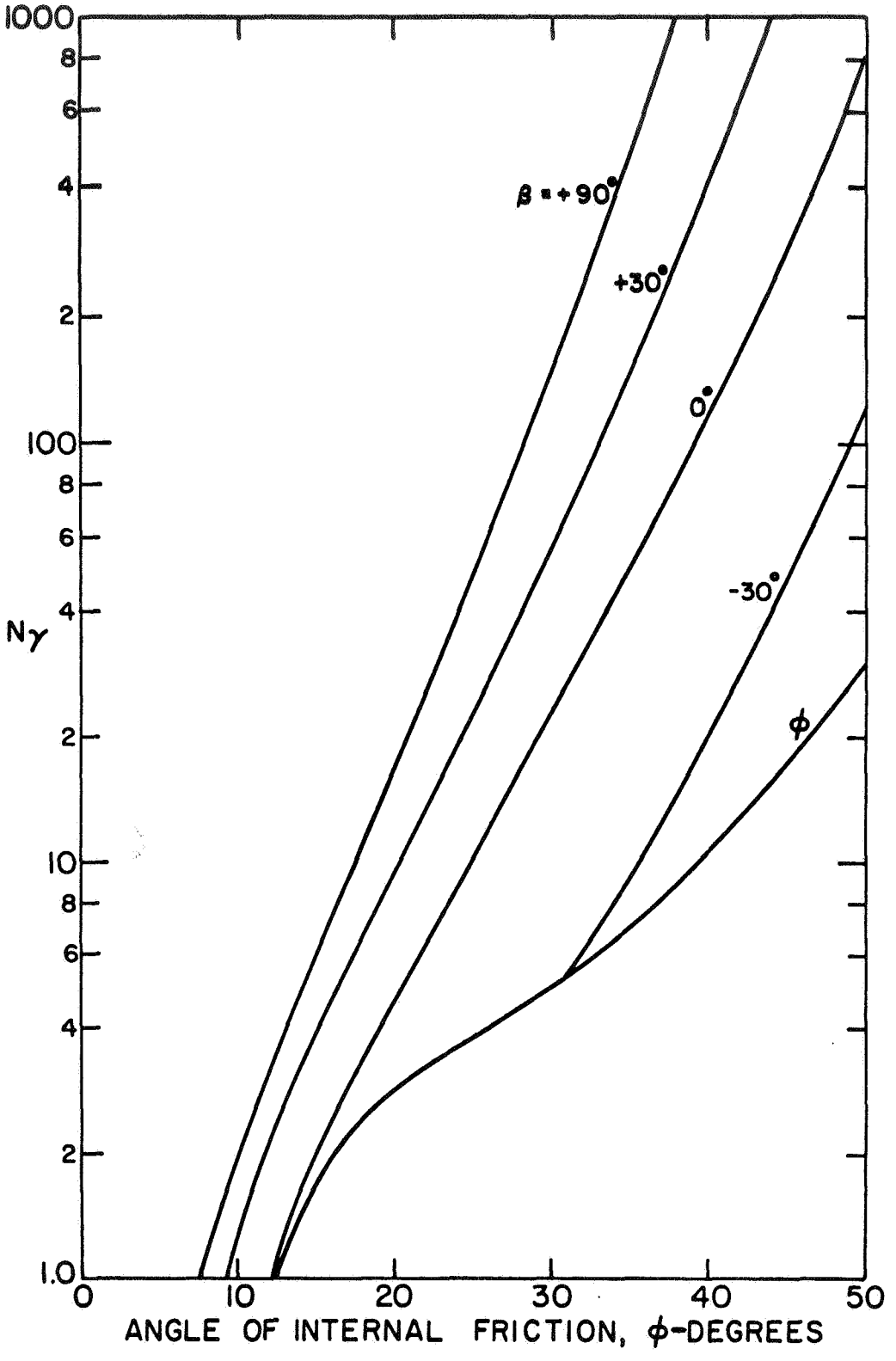

FIGURE 1-6 GENERAL BEARING CAPACITY FACTOR N_c FOR STRIP FOUNDATION (After Meyerhoff, 1951)

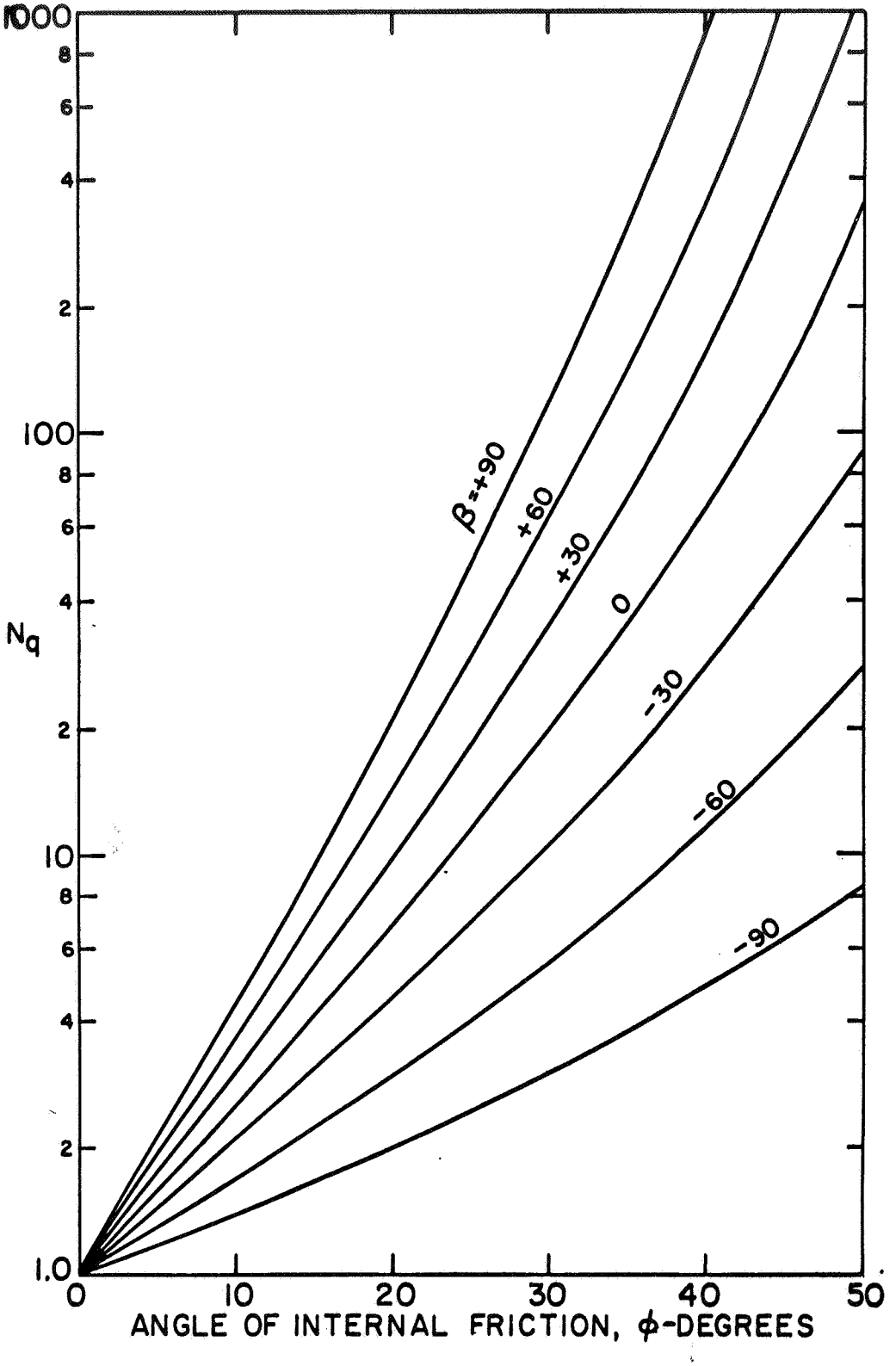

FIGURE 1-7 GENERAL BEARING CAPACITY FACTOR N_c FOR STRIP FOUNDATION (After Meyerhoff, 1951)

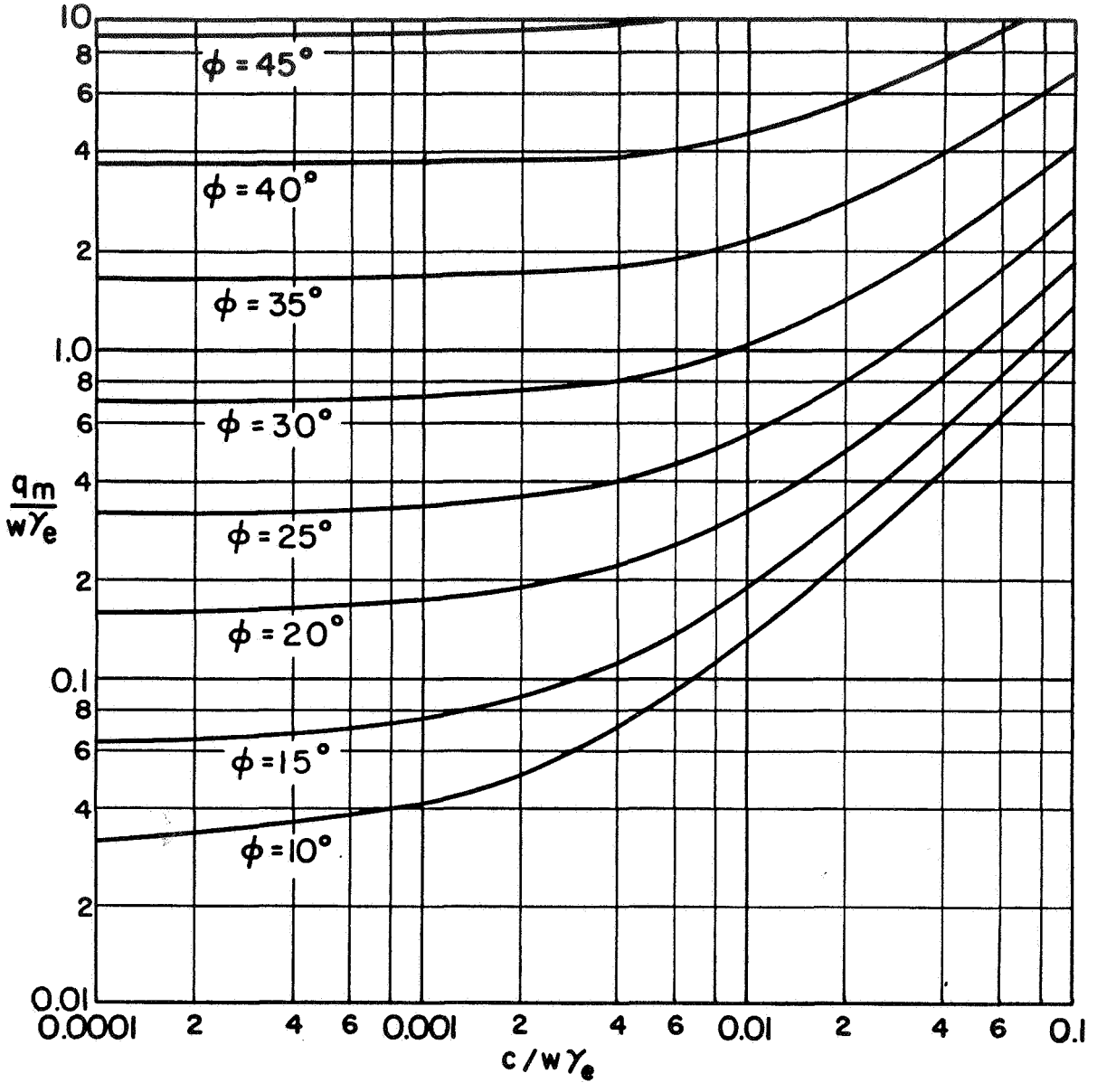

FIGURE 1-8 BEARING CAPACITY RELATION FOR SLOPE ANGLE OF 0° AND NO BOULDER SINKAGE (z/w = 0)

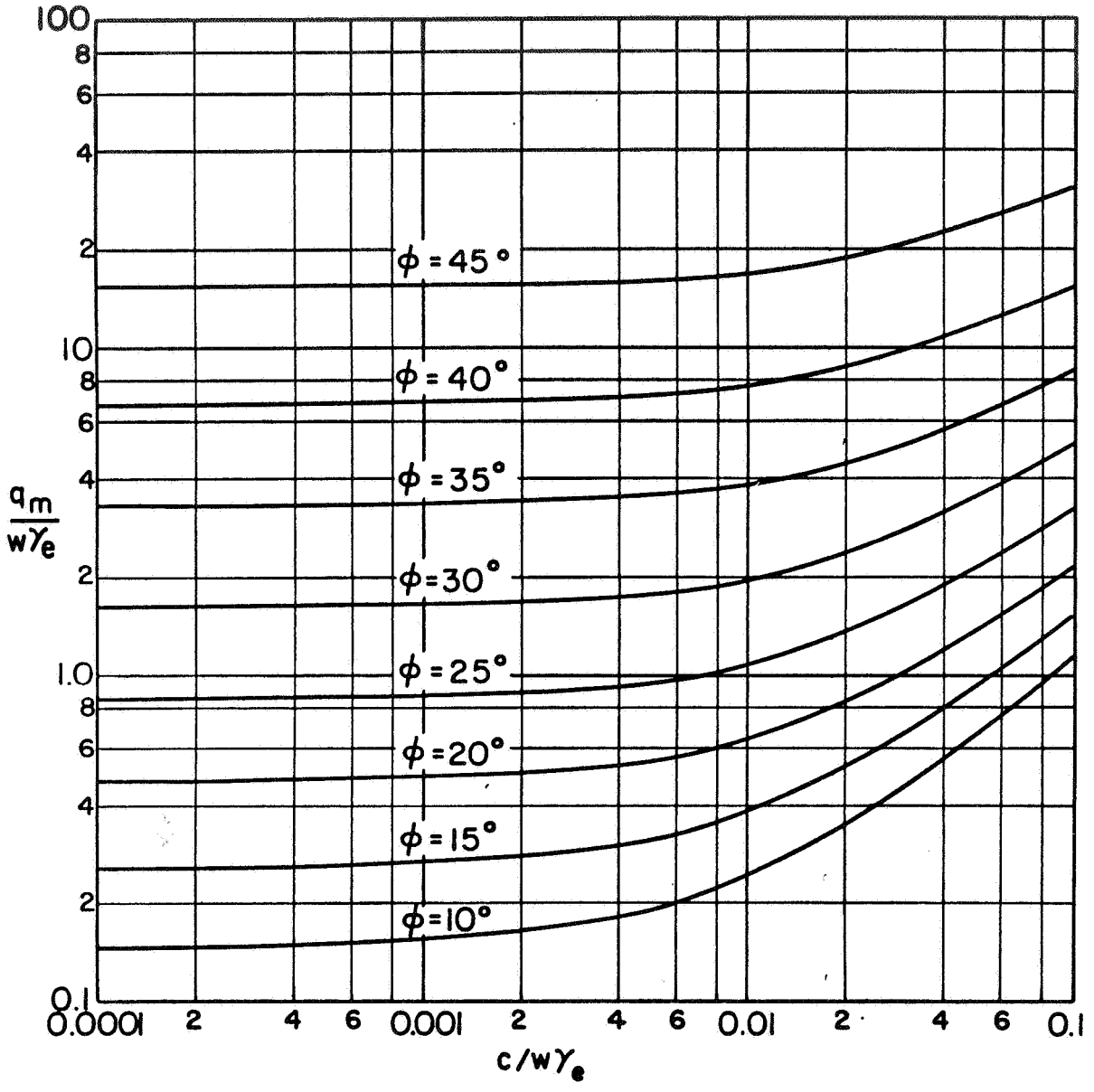

FIGURE 1-9 BEARING CAPACITY RELATION FOR SLOPE ANGLE OF 0° AND BOULDER SINKAGE OF ONE-HALF THE TRACK WIDTH (z/w = 0.5)

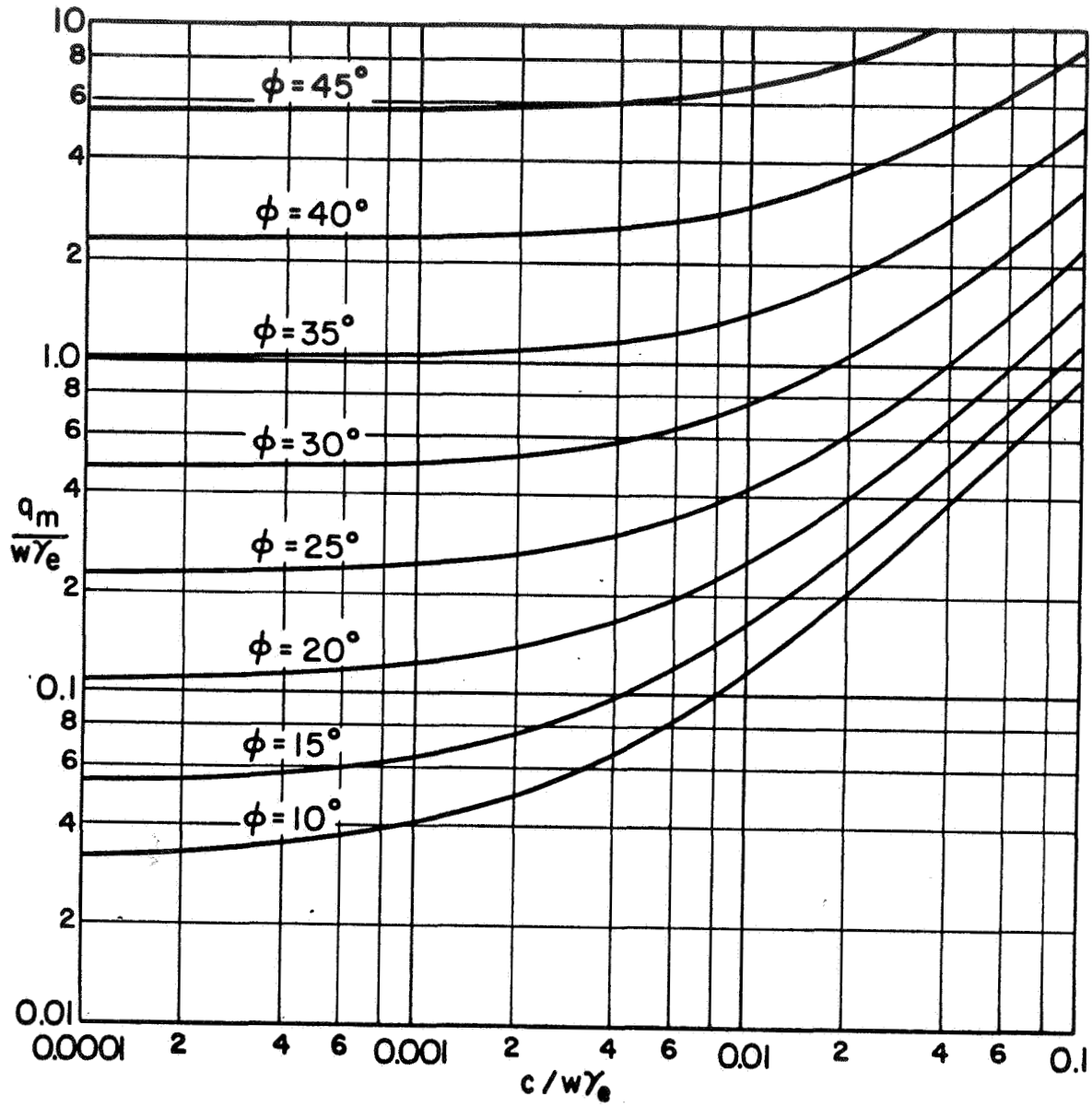

FIGURE 1-10 BEARING CAPACITY RELATION FOR SLOPE ANGLE OF 10° AND NO BOULDER SINKAGE (z/w = 0)

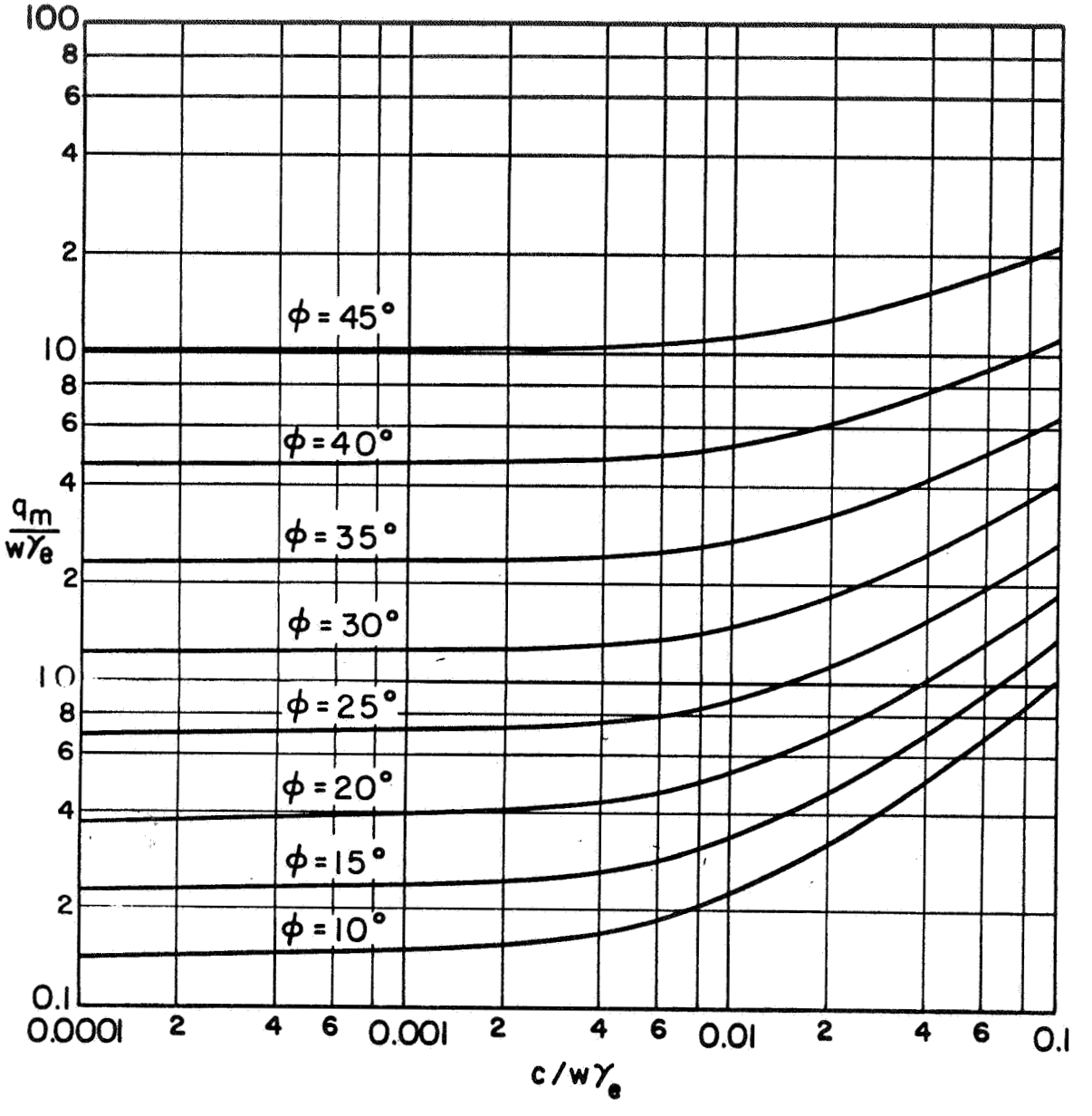

FIGURE 1-11 BEARING CAPACITY RELATION FOR SLOPE ANGLE OF 10° AND BOULDER SINKAGE OF ONE-HALF THE TRACK WIDTH (z/w = 0.5)

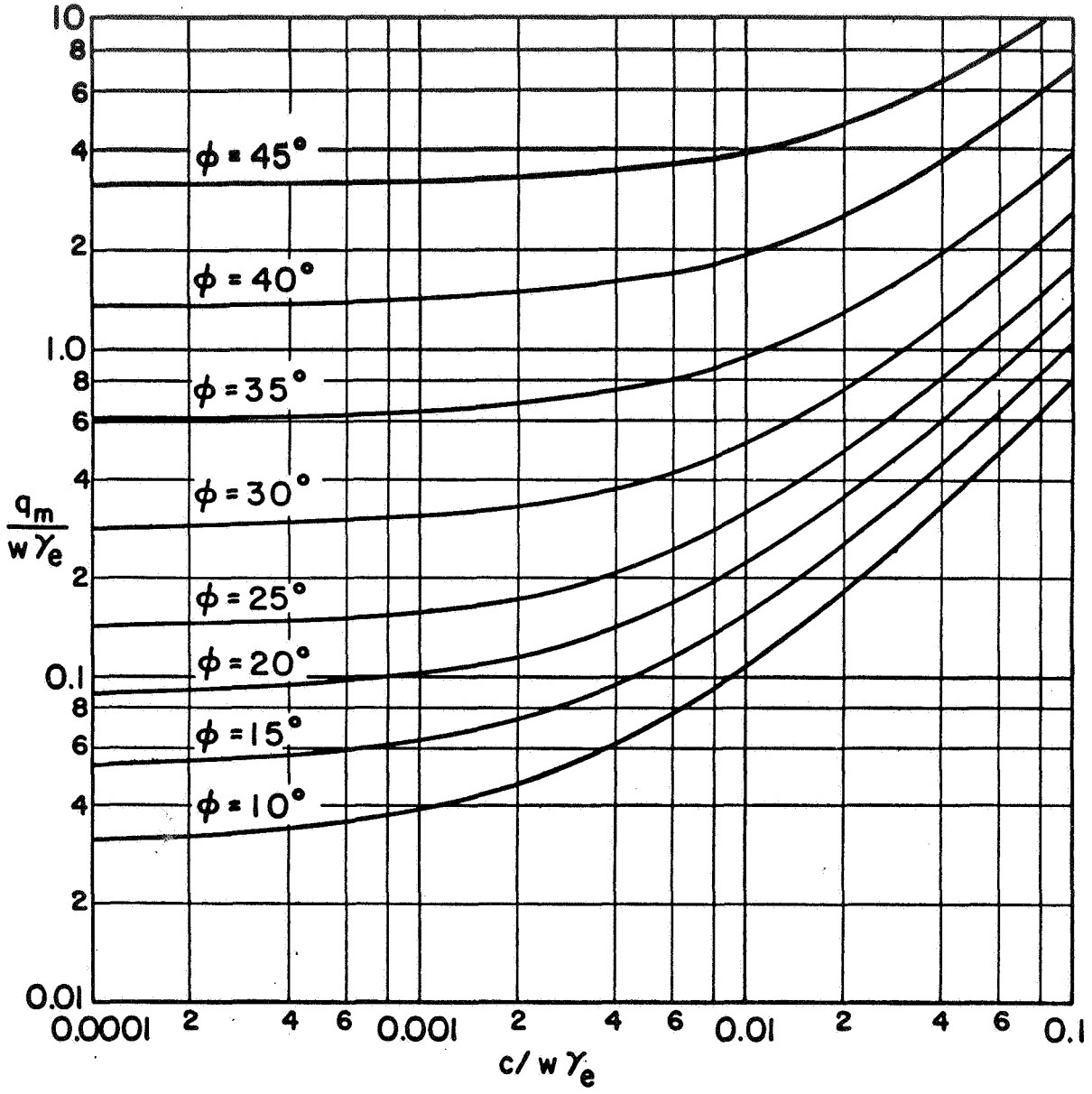

FIGURE 1-12 BEARING CAPACITY RELATION FOR SLOPE ANGLE OF 20° AND NO BOULDER SINKAGE (z/w = 0)

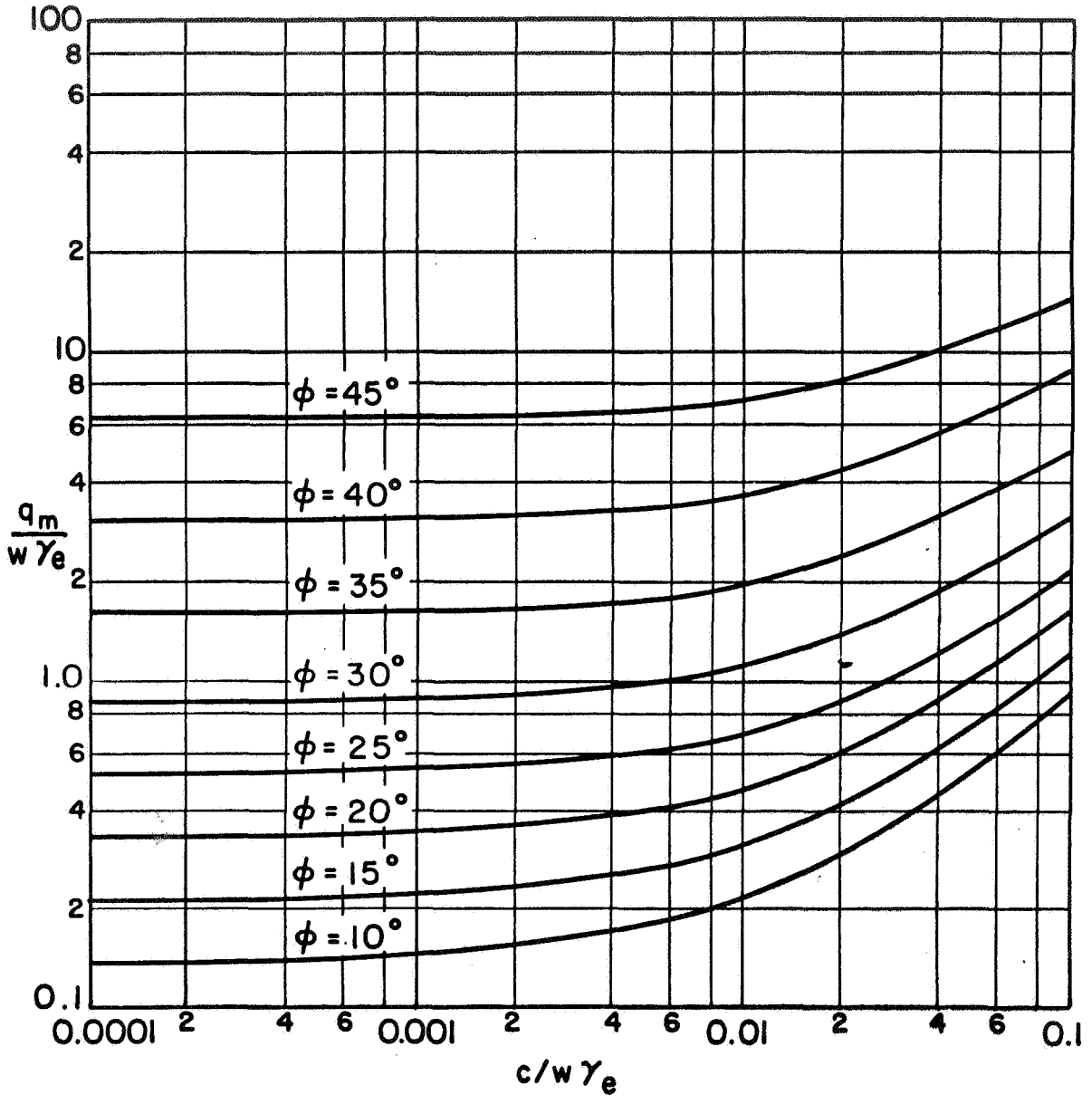

FIGURE 1-13 BEARING CAPACITY RELATION FOR SLOPE ANGLE OF 20° AND BOULDER SINKAGE OF ONE-HALF THE TRACK WIDTH (z/w = 0.5)

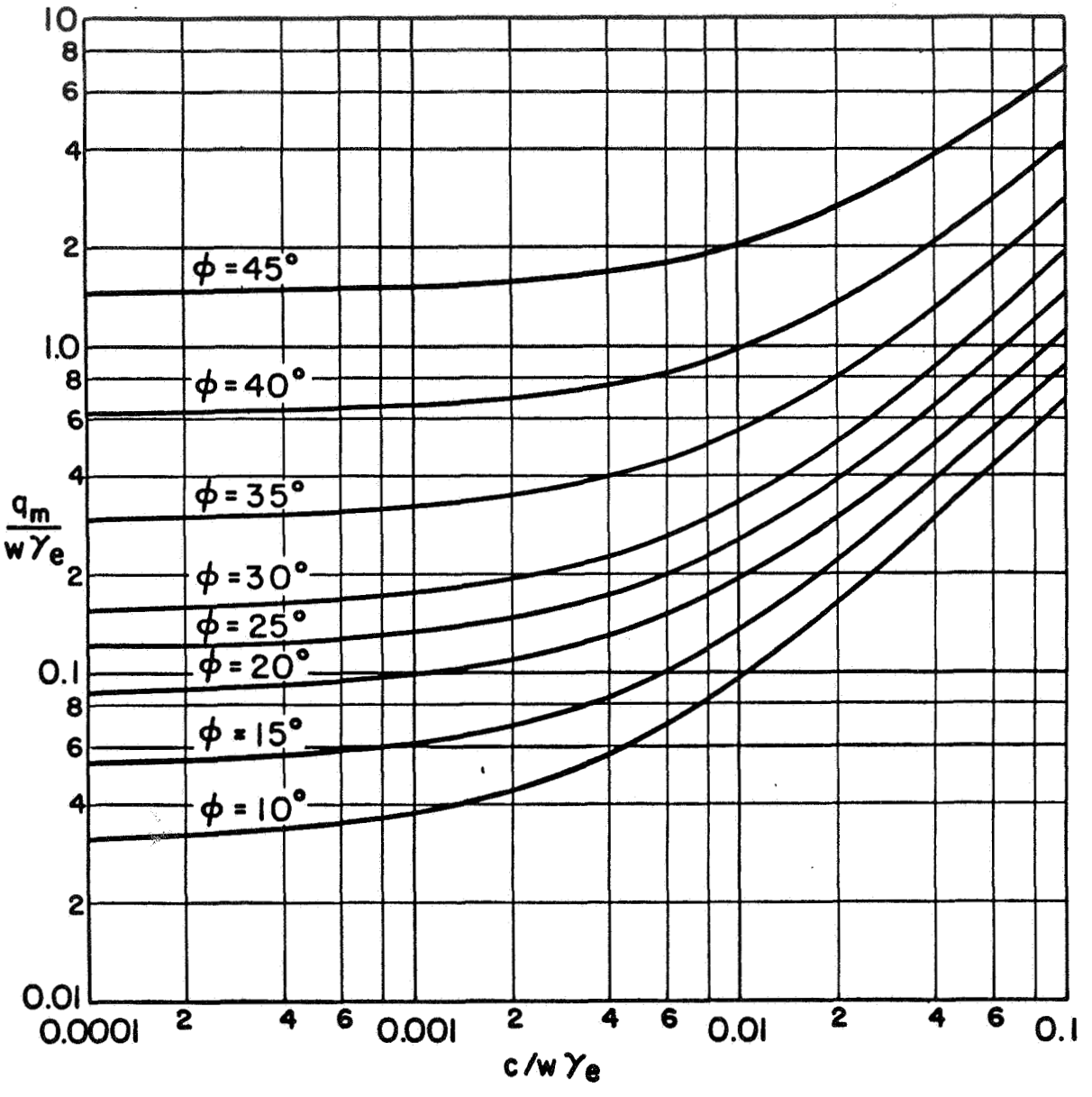

FIGURE 1-14 BEARING CAPACITY RELATION FOR SLOPE ANGLE OF 30° AND NO BOULDER SINKAGE (z/w = 0)

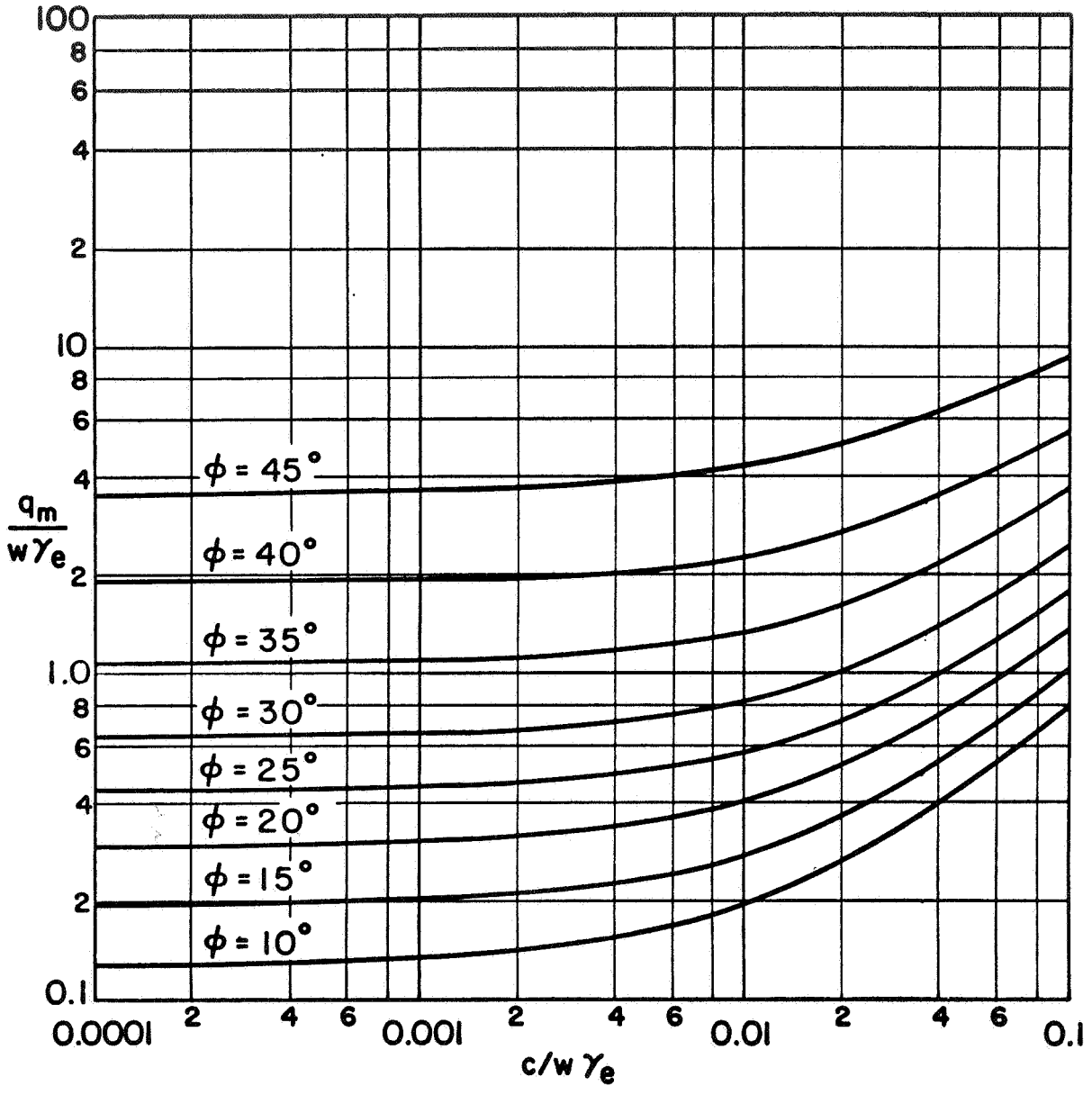

FIGURE 1-15 BEARING CAPACITY RELATION FOR SLOPE ANGLE OF 30° AND BOULDER SINKAGE OF ONE-HALF THE TRACK WIDTH (z/w = 0.5)

where

r = sphere radius

D = sphere diameter, and

γ_r = unit weight of rock.

Dividing both sides of this equation by ($w\gamma$), we have

$$\frac{q}{w\gamma} = \frac{4}{3} \frac{\gamma_{r/\gamma}}{(w/D)^3} \tag{1-12}$$

Again, for the lunar gravity field, lunar soil unit weight equals $\gamma_e/6$. Then the bearing capacity for a sphere in lunar gravity is given by

$$\frac{q_m}{w\gamma_e} = \frac{2}{9} \frac{(\gamma_{r/\gamma})}{(w/D)^3} \tag{1-13}$$

The solution of this equation is presented on Figure 1-16. Hence, the bearing capacity term on the left side of Equation (1-10) is given by Equation (1-13). This term, $q_m/w\gamma_e$, is directly proportional to the density ratio, γ_r/γ, and inversely proportional to the w/D ratio cubed. From the solution of Equation (1-13) and Figures 1-8 to 1-15, ϕ can in most cases be determined directly (the charts are entered with $q_m/w\gamma_e$ and $c/w\gamma_e$ known) or it can be found after simple interpolation between charts.

It is to be noted that Equation (1-10) is an upper bound to bearing capacity, because it gives a solution based on the maximum resistance available for given values of c and ϕ. Equation (1-13) is in principle an exact value of bearing capacity, since for any lower value of q_m the track width would be greater, and for any greater value of q_m the track width would be smaller.

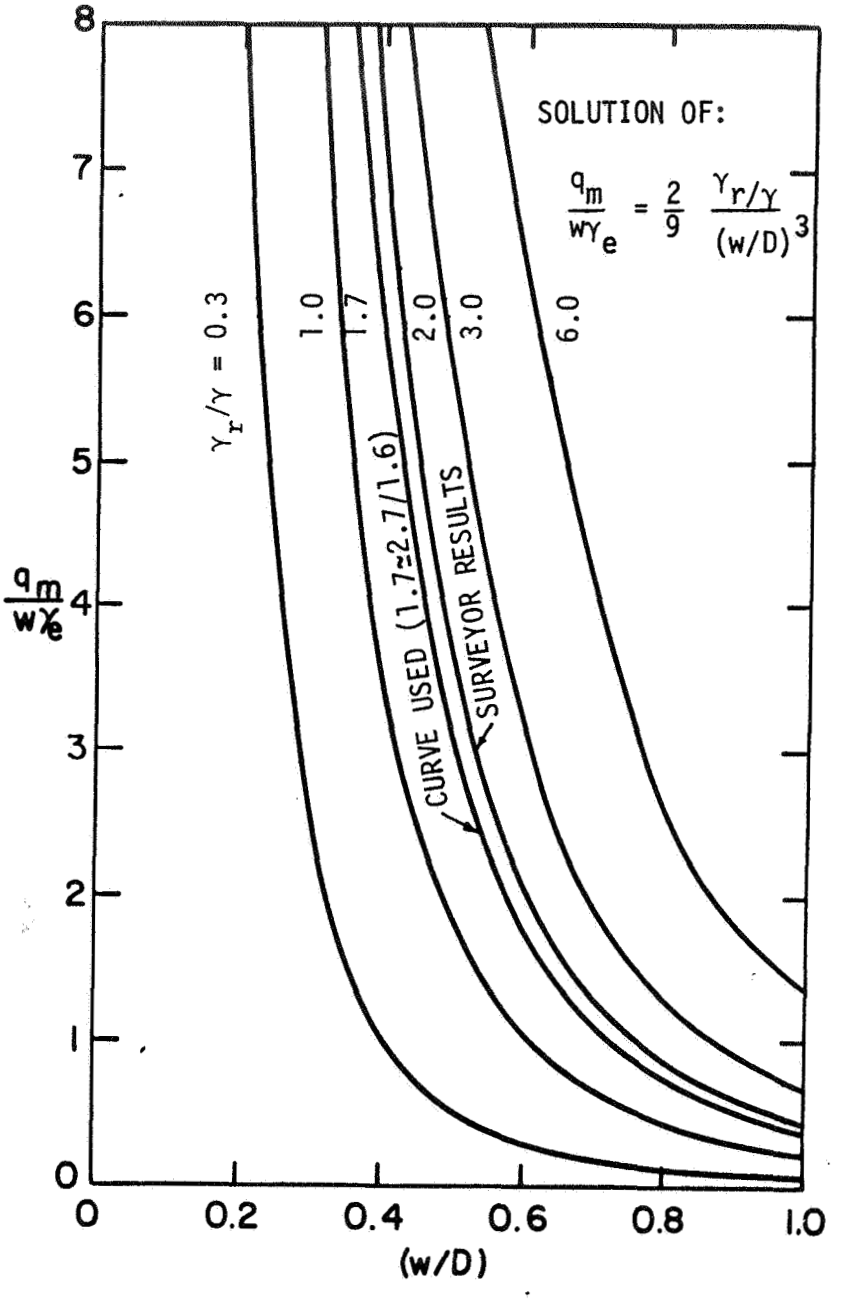

FIGURE 1-16 BEARING CAPACITY = $\frac{\text{weight}}{\text{area}}$ RELATIONSHIP

IV. METHODS USED FOR ANALYSIS OF BOULDER TRACKS

The procedure followed for study of different boulder tracks consisted of (1) locating suitable boulder tracks on high resolution Lunar Orbiter photographs, (2) determining the scale of the photograph or frame, (3) measuring the boulder and track dimensions, (4) estimating the slope angle for selected portions of the track and (5) reviewing tentative geological information to enable better appreciation of assumptions regarding cohesion and density. Some of the above phases of the analysis are described in greater detail below.

A. Scale of the Photographs

The Orbiter Supporting Data* for the Lunar Orbiter missions give the latitude and longitude of 44 equally spaced angles along the photo frame periphery. Points 1, 12, 23, and 34 correspond to the corners of the frame, and can be easily identified. Hence, the distance from one corner to another can be measured on the frame, and the corresponding ground distance can be calculated from the latitude and longitude of the corners given in the supporting data. The scale to be used is then

$$\text{Scale} = \frac{\text{Distance on Frame}}{\text{Distance on Ground}}$$

The distance on the ground is either given in the supporting data or can be determined from geometrical relationships of a sphere. The length of any circular arc on a sphere is given by

$$L_{AB} = \frac{\pi R}{180} \theta_{AB}, \qquad (1\text{-}14)$$

---

* Revised data dated 2-5-69 give the latitude and longitude of additional points including the corners of the frame (Boeing, 1969).

where

L_{AB} = arc distance between points A and B

R = radius of the moon $\cong$ 1740 km

θ_{AB} = angle between A and B.

The geometrical relationships are illustrated on Figure 1-17. By the Pythagorean theorem, neglecting surface curvature, we have for the central angle

$$\theta_{AB} = \sqrt{\theta_{LO}^2 + \theta_{LA}^2},$$

and

$$L_{AB} = \frac{\pi R}{180} \sqrt{\theta_{LO}^2 + \theta_{LA}^2}, \qquad (1\text{-}15)$$

where

$$\theta_{LO} = |a_A - a_b|$$
$$\theta_{LA} = |b_A - b_b|$$

a_A = longitude of point A

b_A = latitude of point A

a_B = longitude of point B

b_B = latitude of point B.

A more correct expression for the distance L_{AB}, which accounts for surface curvature, is given by Roggeveen and Goodman (1968) as

$$L_{AB} = \frac{\pi R}{180} \sqrt{(\theta_{LO} \cos \theta_2)^2 + \theta_{LA}^2}, \qquad (1\text{-}16)$$

where

$$\theta_2 = |b_A - b_B|/2.$$

For central angles less than 3 degrees, $\cos \theta_2 \cong 0.999$. Therefore, for most of the orbiter high resolution photographs where boulder tracks are found, Equation (1-15) is sufficiently accurate.

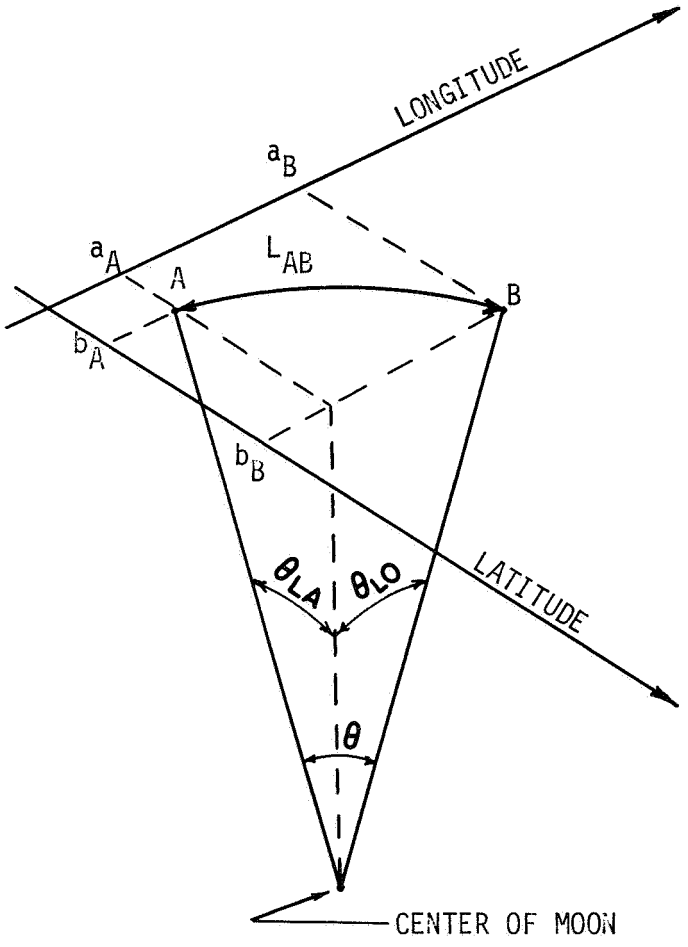

FIGURE 1-17 GEOMETRY FOR DETERMINING ARC LENGTH

The orbiter supporting data give also other information including the camera tilt angle and azimuth, and the scale factor. The scale factor for the high resolution photographs is based on the original size of the frame being approximately 55 mm across and each framelet about 2.54 mm wide. It is understood that these measurements are fairly constant.* If the photograph at hand covers only part of a frame so that measurements cannot be made from corner to corner, the above information makes it possible to determine the scale nevertheless. This is done simply by multiplying the given scale factor by the ratio of framelet width of photograph at hand to 2.54 mm.

These methods were applied for determination of the scale of the photographs used in the analysis.

B. Measurements of Boulder and Track

The boulders and tracks were first measured on high resolution Orbiter frames (approx. 39.8 cm wide). Then the measurements were repeated for most of the boulders on photographs further enlarged having a scale roughly five times that of the high resolution frames. The two measurements were averaged and the resulting values of boulder diameter and track width were used in the analysis. Equal weight was given to both measurements because although objects appeared larger on the enlarged photographs their boundaries were more blurred and harder to define. The two measurements differed from each other by an average of about 10 percent, and the maximum difference was about 30 percent. Such a variation is not surprising, since the smaller boulders were close to the limit of resolution of the photography.

---

* Verbal communication with Dr. Henry J. Moore.

In the analysis of the boulder tracks it was assumed that the boulders were spherical. To make this assumption as valid as possible, only boulders appearing equidimensional on the photographs and leaving relatively smooth and well defined tracks were selected for study.

C. Estimation of Slope Angle

The slope angle was estimated from shadow relationships on the photograph, using the sun angle as listed in the supporting data. For example, if it can be assumed that a boulder is spherical, the slope can be calculated from measurements of boulder diameter, track width, and length of shadow cast by the boulder. This slope will of course be in the direction of the shadow which may not be the direction wanted. A better determination results from the shadow cast by a crater rim or a relatively horizontal upper surface adjacent to a rille. All these methods, however, depend on certain assumptions based on the investigator's interpretation of the photograph and may therefore be considerably in error. These methods were used to estimate the slope angle, α, for the boulders analyzed. Some slope angles were also provided by the USGS through their photogrammetry procedure. It is understood that we may receive additional slope angles from the USGS in the future.

D. Material Properties Used for Analysis of Boulder Tracks

From a review of available data concerning the properties of lunar surface materials (Mitchell et al., 1969), it would appear that the density of soil on the moon may range from 0.6 to 1.2 gm/cc at the surface increasing to 1.5 or 2.0 gm/cc at depth. The density of rock, or solid particles, may range from 2.4 to 3.2 gm/cc with 2.80 or 2.90 gm/cc being given as the most likely average value. Estimates of the cohesion

for lunar soil range from 0.002 to 2 psi, and 0.05 to 0.1 psi was estimated for soil in the Surveyor landing areas. On this basis, and to conform with the values selected by Dr. Moore for similar studies, the following values for soil and rock properties were assumed for this analysis:

	Density gm/cm^3	Unit Weight (Earth) $dynes/cm^3$	Cohesion $dynes/cm^2$
Soil	1.6	1.6×10^3	1×10^3
Rock	2.7	2.7×10^3	——

With the dimensions of the boulder and track thus determined, and material properties selected, friction angle values were determined using the procedure outlined previously.

V. RESULTS

The results of the analysis are presented in Table 1-4. In the framelet column of this table, the first number is the framelet number. The second number signifies the distance in millimeters from the start of that framelet toward the next as measured on the high resolution frames (total frame width is about 39.8 cm). Third number is the distance in millimeters from the data edge.

From Table 1-4 it appears that for most of the boulder tracks analyzed the friction angle is between 27 and 41 degrees. To make it possible to see the general trend of the results more easily, all values were plotted as shown on Figures 1-18 and 1-19. Figure 1-18 shows the relationship between bearing capacity of the soil under the boulder and friction angle of the soil. Figure 1-19 shows the relationship between the track width to boulder diameter ratio and the friction angle.

TABLE 1-4A

Results of Boulder Track Analysis, Orbiter II Photographs

Location	Frame	Framelet (boulder location)	Longitude (degrees)	Latitude (degrees)	Boulder diam. (D) (meters)	Track width (w) (meters)	Slope (α) (degrees)	$\frac{z}{w}$	Bearing capacity (q_m)		ϕ (°)
									(psf)	$\frac{\text{dynes}}{\text{cm}^2} \times 10^5$	
Mare Tranquillitatis (Approx. 100 Km from Apollo Site 1)	II-27H	921	36.54	3.56	6.0	6.0	15	0.50	740	3.55	21
Sabine D (Approx. 30 km from Surveyor 5 and Apollo Site 2)	II-76H*	364	23.68	1.20	8.7	6.4	13	0.23	1970	9.47	32
Sinus Medii (Approx. 20 Km from Surveyor 6 and Apollo Site 3)	II-122H	464	-1.32	0.32	6.3	6.3	15	0.50	770	3.70	21
Sinus Medii (Approx. 20 Km from Surveyor 6 and Apollo Site 3)	II-123H	594 + 15mm, 28mm	-1.89	0.29	5.9	5.4	10	0.35	850	4.09	24

Note: To express bearing capacities in Newton's per square centimeter, multiply the value in dynes/cm^2 by 10^{-5}.

* Slope angle primarily based on slope determined by photogrammetry.

TABLE 1-4B

Results of Boulder Track Analysis, Orbiter III Photographs

Location	Frame	Framelet (boulder location)	Longitude (degree)	Latitude (degree)	Boulder diam. (D) (meters)	Track width (w) (meters)	Slope (α) (degrees)	$\frac{z}{w}$	Bearing capacity (q_m)		ϕ
									psf	$\frac{\text{dynes}}{\text{cm}^2} \times 10^5$	(°)
Mare Fecunditatis (Approx. 150 Km WNW of Messier A)	III-35H	396 + 4 mm, 258mm	42.81	-1.05	5.0	4.6	25	0.35	725	3.48	27.5
N E Mösting	III-107H	868 + 1mm, 21mm	-5.67	-0.33	3.6	2.8	10	0.23	725	3.48	30
Rima Hipparchus	III-111H	364 + 1mm, 286mm	4.83	-4.92	5.2	5.2	30	0.50	640	3.07	22.5
		373 + 13mm, 392mm			6.0	4.9	10	0.26	1100	5.28	27
Reinhold (Approx. 30Km E. of Reinhold K)	III-125H	204 + 1.5mm, 69mm	-20.04	-0.60	2.3	1.6	15	0.21	580	2.78	33
		204 + 3mm, 75mm			2.5	2.5	15	0.50	310	1.49	20
		204 + 5mm, 76mm			2.5	1.9	15	0.23	530	2.54	31
		205 + 13mm, 53mm			2.7	2.1	15	0.23	550	2.64	31
		206 + 15mm, 64mm			4.1	3.7	20	0.31	610	2.93	28
Oceanus Procellarum (Approx. 40 Km from Surveyor 1)	III-181H	567 + 7mm, 284mm	-43.54	-2.11	3.2	2.2	10	0.21	830	3.98	32
Oceanus Procellarum (Approx. 40 Km from Surveyor 1)	III-189H	615 + 1mm, 77mm	-44.17	-2.41	2.9	2.4	5	0.27	520	2.50	26
		617 + 7mm, 91mm			6.2	5.1	5	0.28	1130	5.41	26

TABLE 1-4C

Results of Boulder Track Analysis, Orbiter V Photographs

Location	Frame	Framelet (boulder location)	Longitude (degrees)	Latitude (degrees)	Boulder diam. (D) (meters)	Track width (w) (meters)	Slope (α) (degrees)	$\frac{z}{w}$	Bearing capacity (q_m) psf	Bearing capacity (q_m) $\frac{dynes}{cm^2} \times 10^5$	φ (°)
Central mountains of Petavius (rille)	V-34H	880 + 12mm, 176mm	60.57	-25.70	23.3	13.7	20	0.16	8400	40.40	38
		891 + 6mm, 146mm			19.0	13.7	20	0.21	4500	21.60	34
Mare Tranquillitatis (Approx. 40 Km west of Censorinus)	V-63H	738 + 14mm, 147mm	32.75	-0.44	7.35	4.8	0	0.18	2110	10.10	32
		738 + 16mm, 147mm			8.2	6.0	0	0.23	1910	9.17	29
Large hill south of Alexander	V-88H**	011 + 8.5mm, 230mm	13.54	38.92	19.5	10.6	20	0.15	8150	39.20	42
S. E. part of Hyginus	V-95H*	942 + 18mm, 365mm	5.94	7.56	13.1	8.8	30	0.19	3600	17.30	41
		957 + 11.5mm, 164mm			8.9	6.2	15	0.20	2270	10.90	34
		959 + 12.5mm, 161mm			9.5	5.6	15	0.17	3360	16.10	38
		962 + 3mm, 167mm			8.6	4.6	15	0.15	3690	17.70	40
		965 + 11mm, 239mm			10.0	5.7	15	0.16	3800	18.30	38
		968 + 13mm, 253mm			11.2	4.2	20	0.11	9760	47.00	47
		970 + 7mm, 246mm			14.4	9.2	20	0.18	4350	20.90	38
		978 + 13mm, 252mm			6.0	4.8	15	0.25	1160	5.58	30
		960 + 9mm, 146mm			4.9	4.9	30	0.50	600	2.88	22

**Photogrammetrically determined slope is about 30°: 20° slope is primarily based on shadow technique.

TABLE 1-4C (contd)

Location	Frame	Framelet (boulder location)	Longitude (degrees)	Latitude (degrees)	Boulder diam. (D) (meters)	Track width (w) (meters)	Slope (α) (degrees)	w/D	Bearing capacity (q_m) psf	Bearing capacity (q_m) $\frac{dynes}{cm^2} \times 10^5$	ϕ (°)
N E part of Hyginus	V-96H*	092 + 1mm, 46mm	5.96	7.85	15.9	10.6	10	0.19	4410	21.20	34
N E part of Hyginus	V-97H	175 + 11mm, 268mm	5.98	8.14	11.0	5.7	15	0.14	5040	24.30	40
		175 + 13mm, 275mm			7.6	4.3	25	0.15	2900	14.00	41
		178 + 10mm, 224mm			7.1	4.3	10	0.17	2370	11.40	36
		178 + 14mm, 222mm			7.1	4.0	10	0.16	2760	13.30	36
		180 + 5mm, 230mm			6.2	4.3	15	0.20	1580	7.60	34
		180 + 4mm, 229mm			7.6	4.8	15	0.17	2340	11.30	36
		180 + 1mm, 235mm			7.1	5.2	15	0.21	1620	7.80	33
Hadley Rille	V-105H*	233 + 8mm, 232mm	2.95	25.00	14.9	9.6	25	0.19	4400	21.20	39
		233 + 11mm, 234mm			13.5	8.9	15	0.19	3820	18.40	35
		234 + 8mm, 235mm			13.2	8.6	5	0.19	3830	18.50	33
Rima Bode	V-122H	475 + 9mm, 121mm	-3.97	12.92	12.2	9.0	15	0.22	2770	13.40	32
Copernicus (center)	V-151H	280 + 17mm, 184mm	-20.34	9.42	9.1	6.6	10	0.21	2130	10.30	32
		315 + 11mm, 282mm			12.2	5.5	5	0.12	7350	35.40	40

TABLE 1-4C (contd)

Location	Frame	Framelet (boulder location)	Longitude (degrees)	Latitude (degrees)	Boulder diam. (D) (meters)	Track width (w) (meters)	Slope (α) (degrees)	$\frac{w}{D}$	Bearing Capacity (q_m)		ϕ
									psf	$\frac{dynes}{cm^2} \times 10^5$	(°)
Copernicus (NW of center)	V-155H	845 + 14mm, 340mm	-20.24	10.58	10.6	4.8	0	0.12	6300	30.40	39
Copernicus (NW of center)	V-156H	962 + 8mm, 135mm	-20.21	10.87	11.9	10.7	10	0.32	1800	8.68	27
Center of Vitello	V-168H	518 + 9mm, 188mm	-37.57	-30.61	19.2	19.2	15	0.50	2360	11.40	21
		519 + 1mm, 185mm			11.4	5.4	10	0.12	6200	29.90	41
		520 + 2mm, 184mm			8.0	4.8	15	0.17	2730	13.20	37
		520 + 9mm, 188mm			11.9	7.9	15	0.19	3310	16.00	35
North rim of Gassendi	V-179H	972 + 7mm, 250mm	-39.97	-16.29	8.6	5.5	15	0.18	2580	12.45	34
		972 + 15mm, 333.4mm			5.6	5.3	15	0.35	765	3.69	25
		972 + 15.2mm, 338mm			5.4	4.7	15	0.31	880	4.25	27
		005 + 15mm, 244mm			16.4	14.1	15	0.29	2720	13.10	29
		973 + 10mm, 345mm			9.4	6.0	10	0.18	2830	13.70	34
		973 + 3mm, 285mm			6.8	6.0	20	0.29	1080	5.20	30
		977 + 10mm, 340mm			16.0	14.0	15	0.30	2570	12.40	29
		977 + 17mm, 325mm			7.0	6.1	20	0.28	1140	5.50	30
		977 + 17mm, 305mm			5.6	5.0	25	0.31	860	4.15	30
		979 + 6mm, 352mm			7.5	4.8	10	0.19	2250	10.90	34

TABLE 1-4C (contd)

Location	Frame	Framelet (boulder location)	Longitude (degrees)	Latitude (degrees)	Boulder diam. (D) (meters)	Track width (w) (meters)	Slope (α) (degrees)	w/D	Bearing Capacity (q_m)		ϕ
									psf	$\frac{\text{dynes}}{\text{cm}^2} \times 10^5$	(°)
Schröter's Valley	V-203H	111 + 7mm, 246mm	-49.51	25.13	7.4	5.4	10	0.22	1700	8.20	31
		111 + 7mm, 246mm			7.4	5.4	20	0.22	1700	8.20	35
Schröter's Valley	V-203H*	227 + 8mm, 41mm	-49.48	25.52	9.4	6.2	15	0.19	2640	12.70	35
		221 + 18mm, 161mm			12.6	6.5	5	0.14	5800	28.00	38
		210 + 15mm, 242mm			12.6	7.2	15	0.16	4750	22.90	39
		210 + 14mm, 177mm			10.5	5.5	25	0.14	4670	22.50	44
		202 + 7mm, 253mm			19.4	12.3	20	0.18	5930	28.60	38
Oceanus Procellarum (Approx. 130 Km NW of Marius)	V-213H	417 + 7mm, 294mm	-56.03	13.50	7.4	4.3	20	0.16	2710	13.10	40
		431 + 10mm, 290mm			6.4	3.3	15	0.14	2940	14.20	41

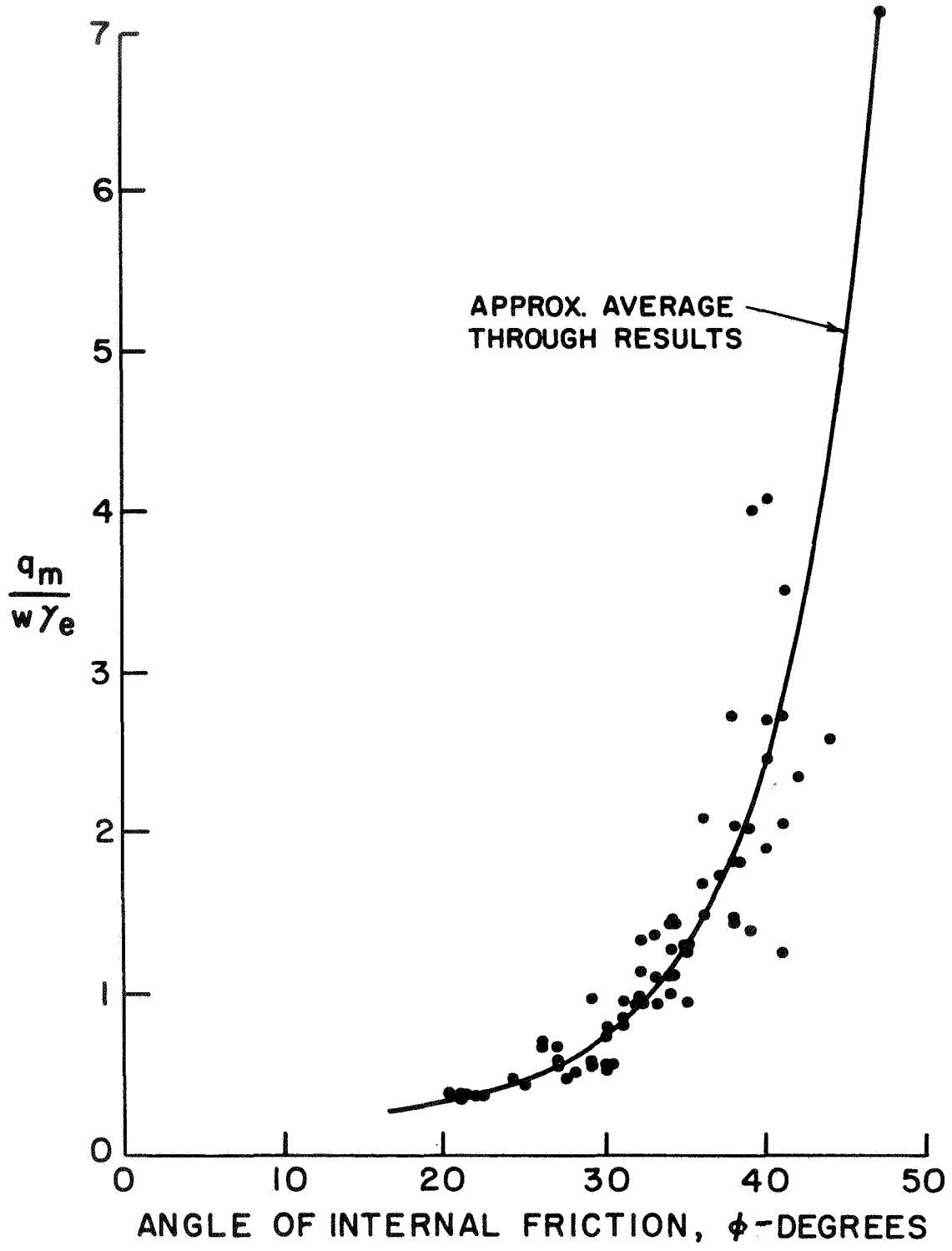

FIGURE 1-18 BEARING CAPACITY VS FRICTION ANGLE

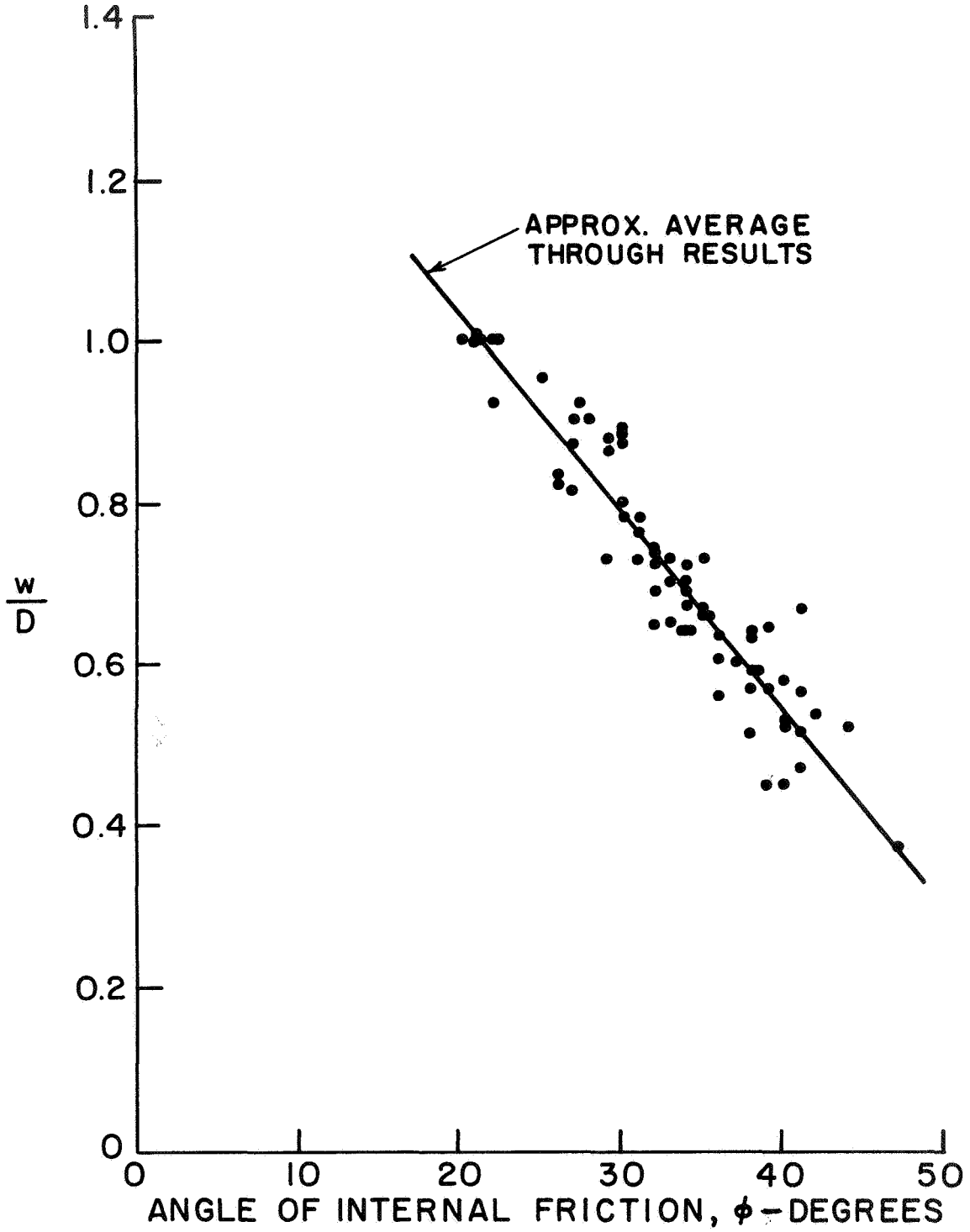

FIGURE 1-19 TRACK WIDTH OVER DIAMETER RATIO VS FRICTION ANGLE

To demonstrate the influence of the slope angle, α, theoretical curves were plotted with the results as shown on Figures 1-20 and 1-21. These curves were obtained by using $\gamma_r/\gamma = 1.7$ and the approximate average of all boulders analyzed for other dimensionless parameters which were:

$$\left(\frac{c}{w\gamma_e}\right)_{ave.} = 0.001$$

$$\left(\frac{z}{w}\right)_{ave.} = 0.234$$

The statistical average for all values of friction angle was found to be 33 degrees. The number of results of ϕ, or range of ϕ, is shown on Figure 1-22. This figure shows that most of the results center around a friction angle of 34 degrees.

VI. DISCUSSION

A number, ϕ, which has been defined as the apparent friction angle, has been computed for lunar soils in this analysis. This has been based on a relationship which has been assumed to exist between lunar boulders and the tracks they left as they rolled down slopes. It is to be emplasized that whether this number, ϕ, is actually the friction angle of lunar soils or only an index parameter somehow related to the friction angle of lunar soil remains to be seen.

As shown in Table 1-4 and on Figure 1-22a, ϕ varied considerably - from 20 to 47 degrees - although the bulk of the results centered around 34 degrees. In some locations, the measurements indicated a significant variability within the same slope. That is, the sinkage, z/w, of one boulder was significantly greater than an adjacent boulder also analyzed

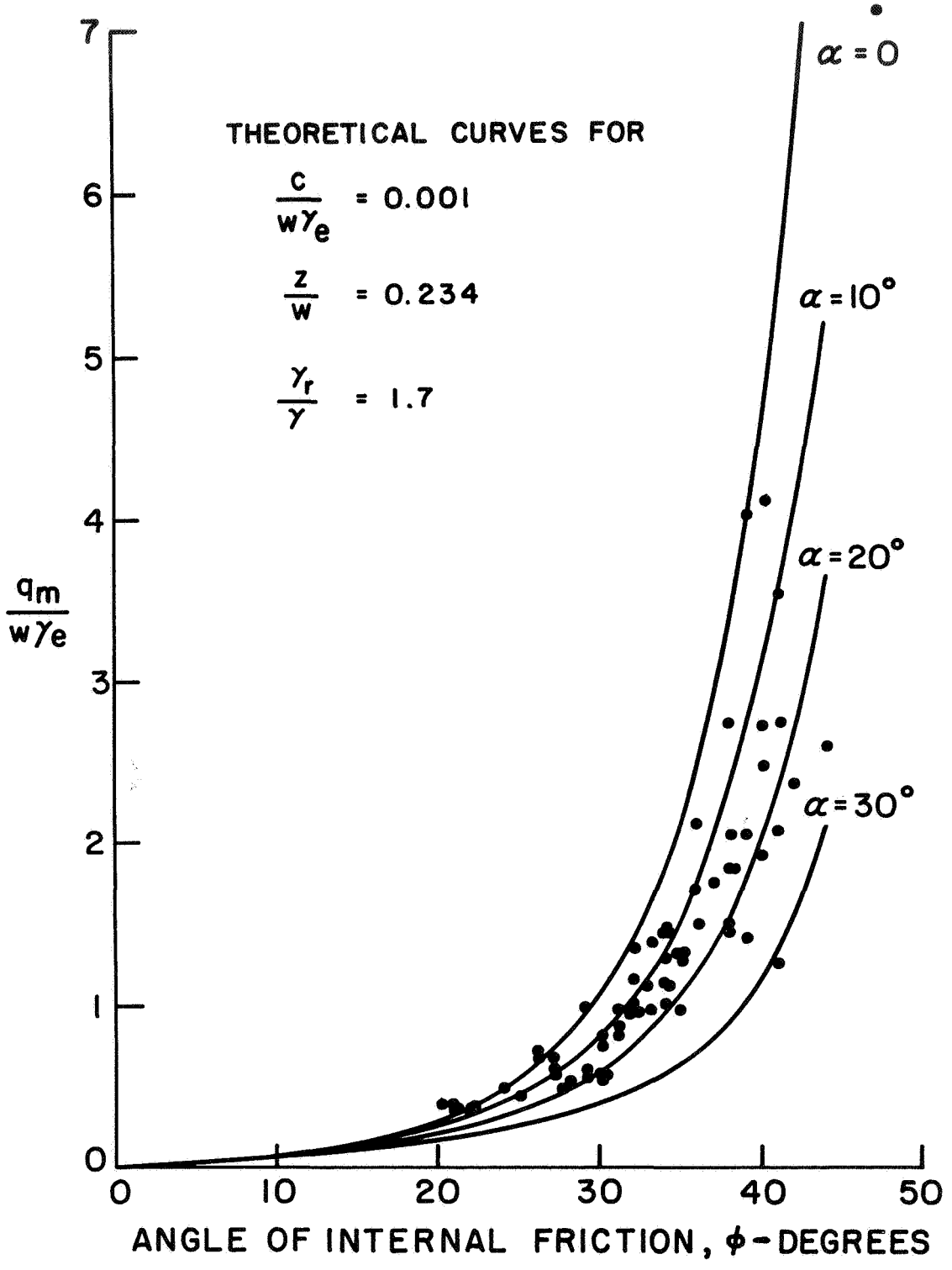

FIGURE 1-20 BEARING CAPACITY VS FRICTION ANGLE SHOWING INFLUENCE OF SLOPE ANGLE

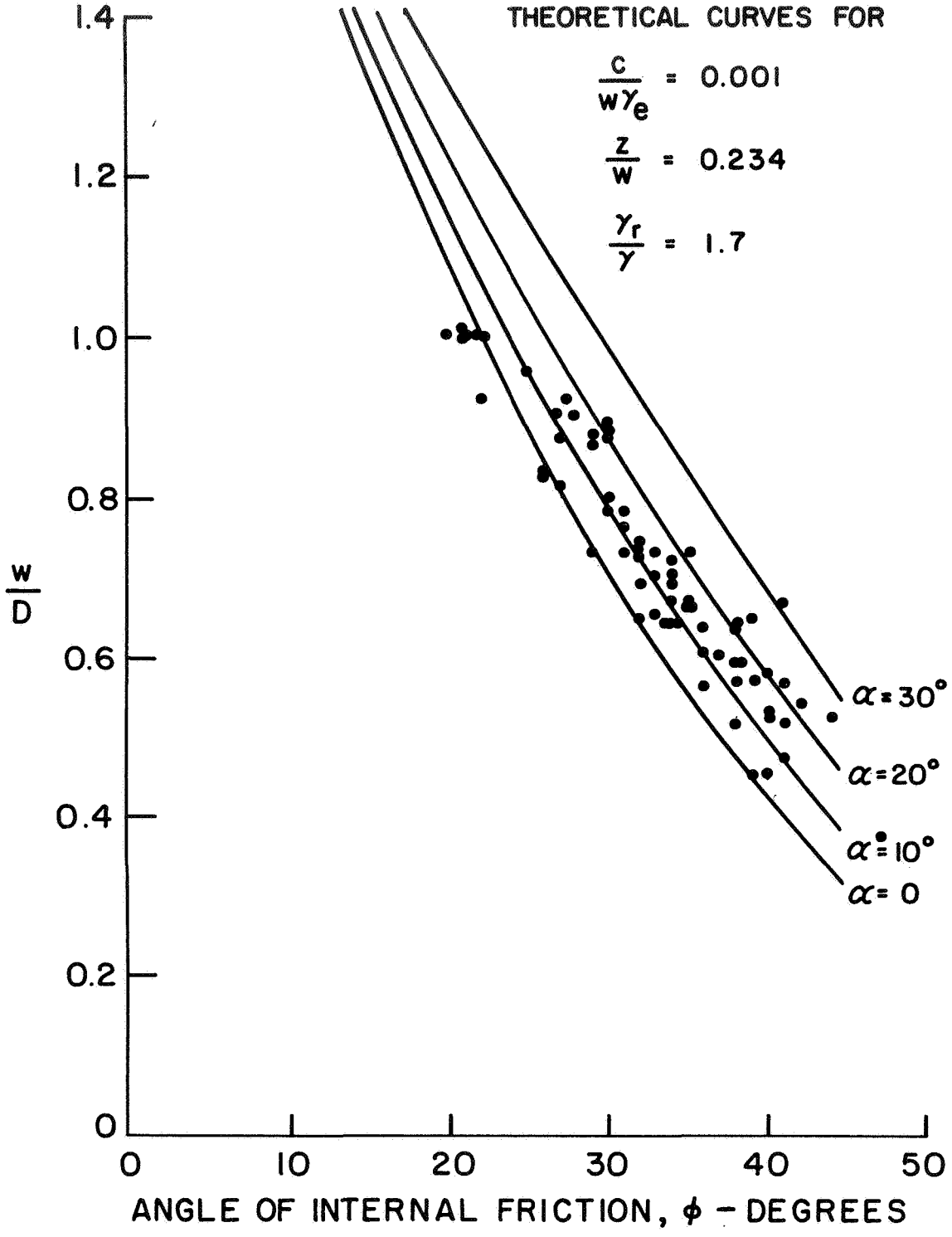

FIGURE 1-21 w/D RATIO VS FRICTION ANGLE SHOWING INFLUENCE OF SLOPE ANGLE

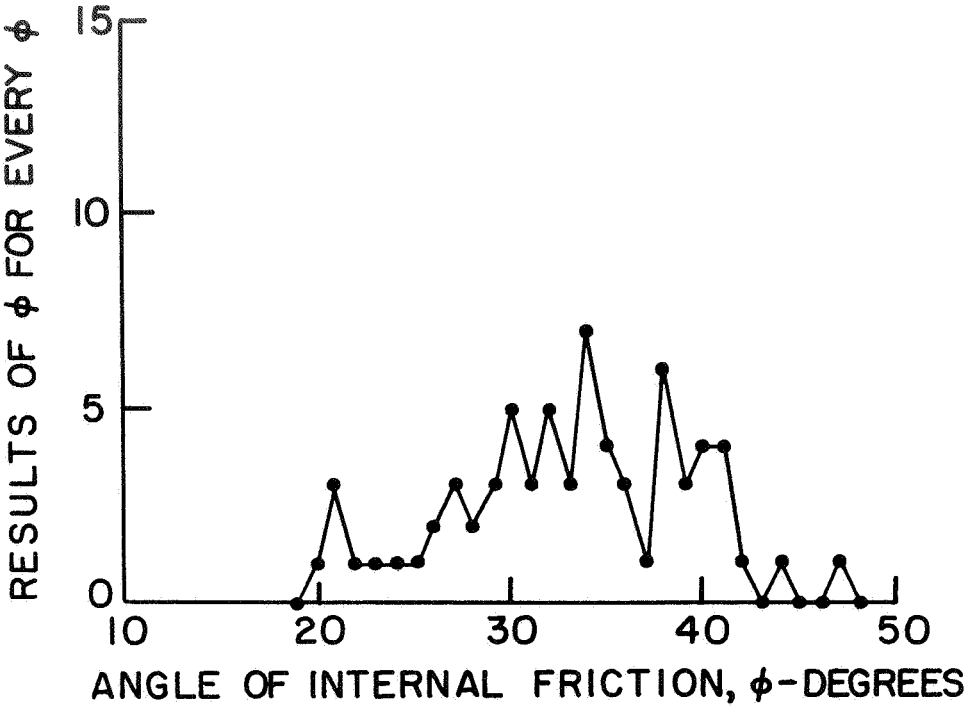

(a)

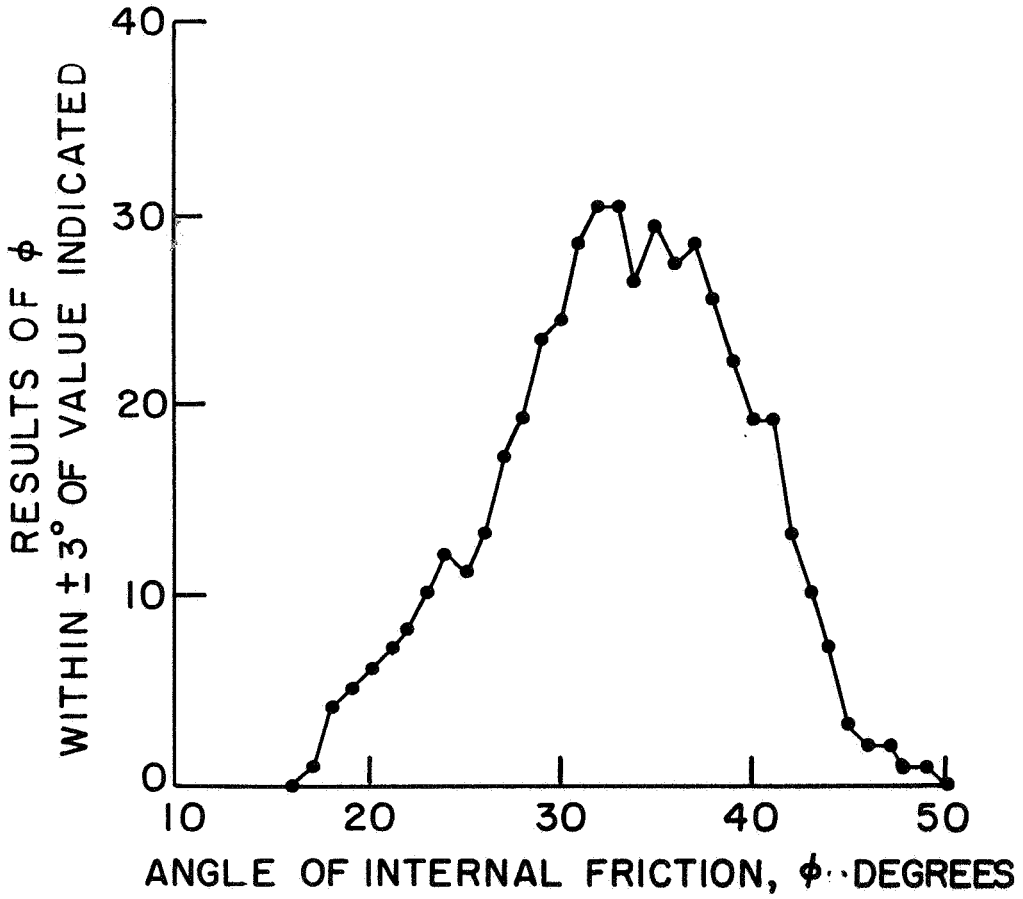

(b)

FIGURE 1-22 FREQUENCY DISTRIBUTION OF THE RESULTS

(Frames III-125H, V-95H, and V-168H). Possible interpretations for such variations would be that (1) the soil properties differed at the two locations, (2) the boulder causing the track somehow did not conform to the assumptions of the theory used; perhaps it was not spherical or it had inertial energy beyond that assumed, and (3) other as yet unknown causes. For most of the locations, on the other hand, the results were more constant.

For many tracks, the measured track width, w, was equal to the boulder diameter, D. Hence, we can conclude that in such cases the thickness of unconsolidated soil on the slope must have been close to or more than half the boulder diameter.

Since the Surveyor results quite consistently indicate that the friction angle for lunar soil may be in the range of 37 to 39 degrees (Surveyor VII Mission Report, 1968), it is of interest to consider possible causes of the considerably larger range found here. As stated before, the results of this analysis indicate an average ϕ of 34 degrees with a range from 20 to 47°. It is appropriate, however, to assess the degree of confidence that may be placed in these results.

A. Implications of Geology

From the review (Section II) of the geology of boulder track locations and on observations made on the orbiter photographs, boulders and boulder tracks are usually associated with slopes where active erosion appears to be taking place; rilles, young large craters, and slopes with fresh rock outcrops are typical. Such slopes are illustrated on Figures 1-23 and 1-24. Figure 1-23 shows boulder tracks studied in Hadley Rille. Note that the tracks can be traced up the slope to the rock outcrop but not above. Figure 1-24 shows boulder tracks in

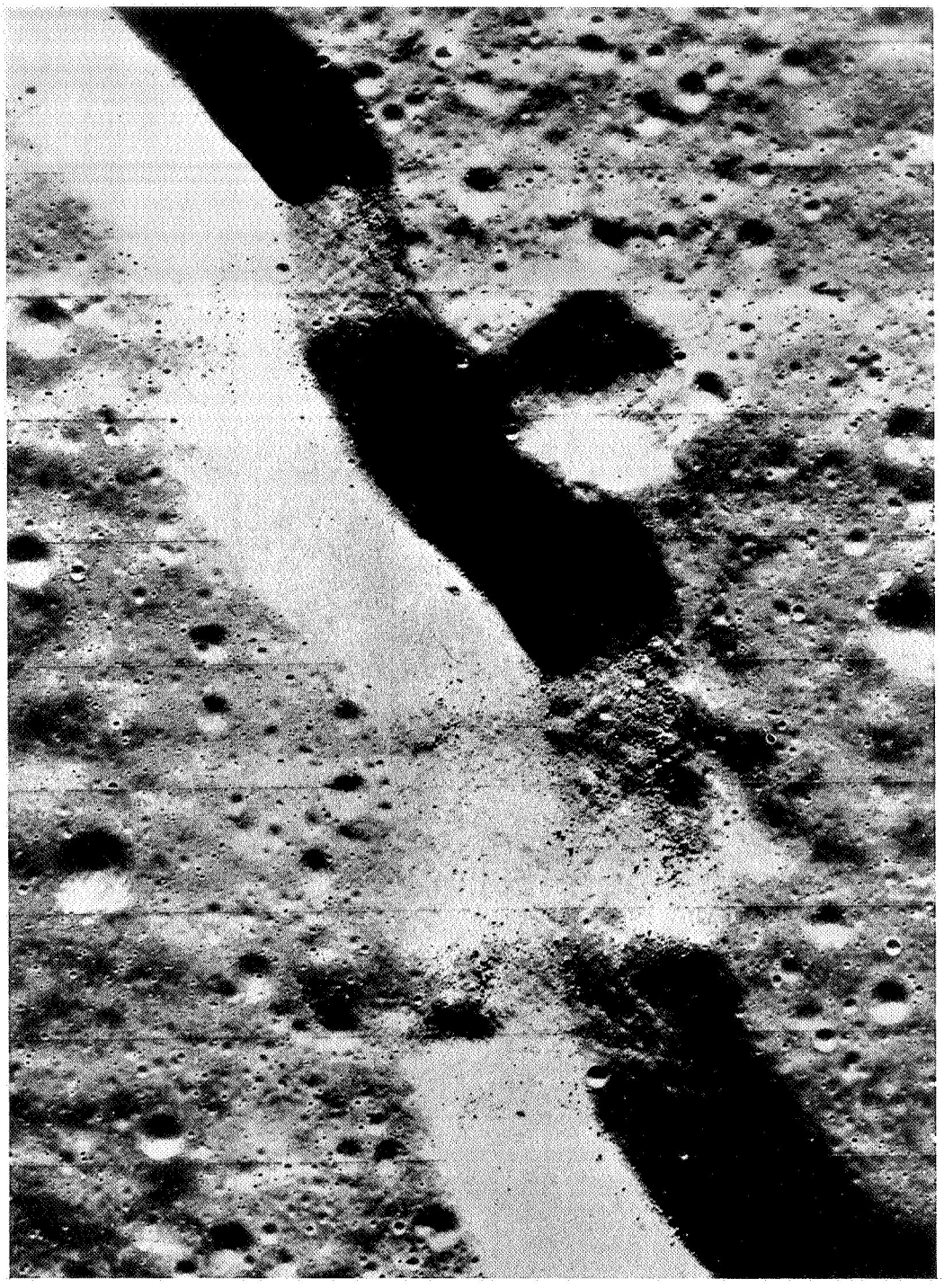

FIGURE 1-23 BOULDER TRACKS IN HADLEY RILLE

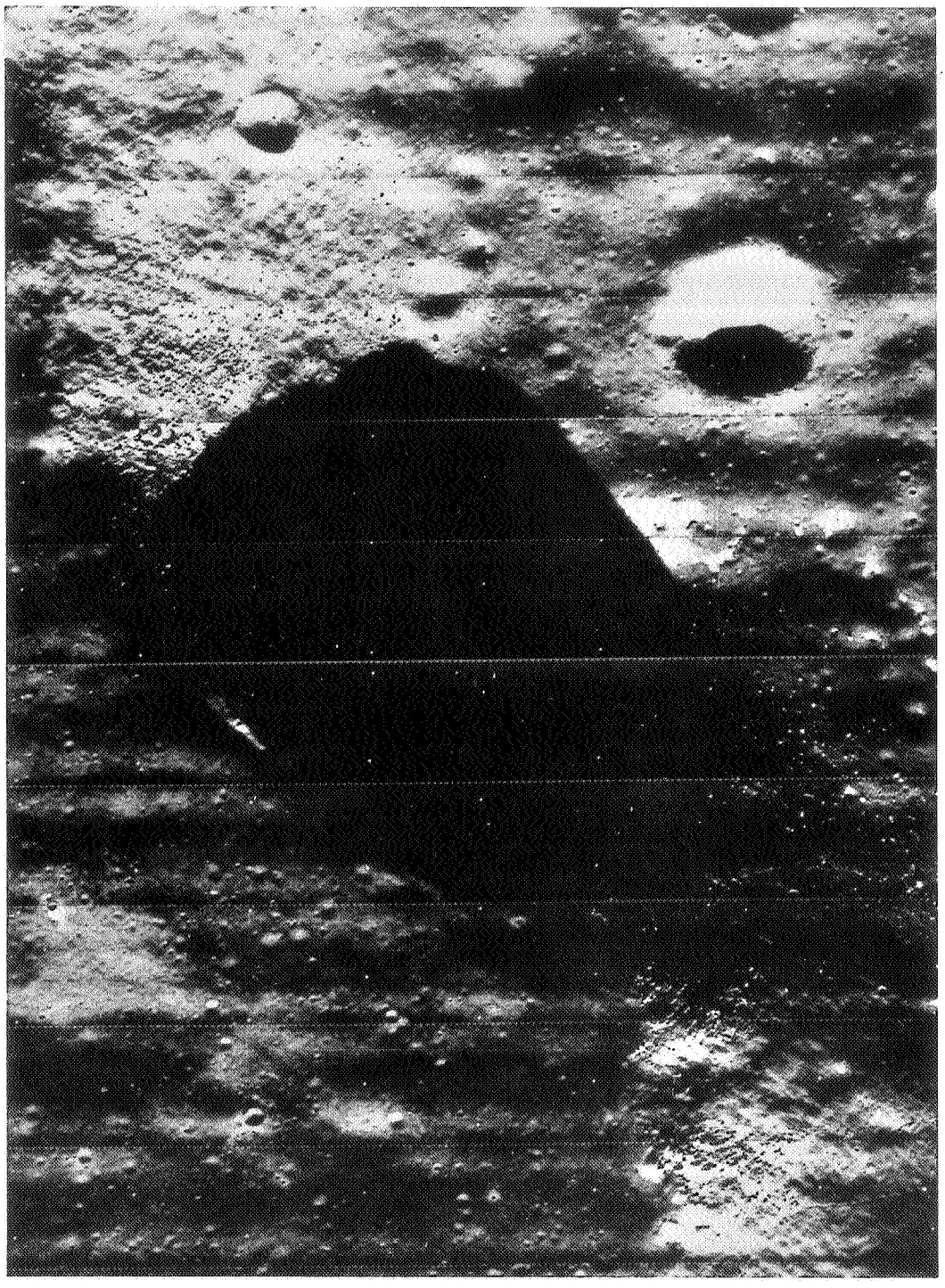

FIGURE 1-24 BOULDER TRACKS IN HYGINUS

Hyginus. It appears that many boulders originate at a rock outcrop from which they loosen and separate, perhaps due to shock, removal of support, and cracking caused by temperature changes.

With such a location described as general for the boulder tracks, the question arises as to what these slopes of colluvium are representative of; i.e., are they representative of the fragmental surface of the moon in general? Analysis of the Surveyor landing sites indicates that the rock grain density of maria is about 3.2 gm/cc and that of the highland areas about 3.0 gm/cc (Surveyor VII Mission Report, 1968). Although this difference is significant in implying a somewhat different composition of maria and upland rocks, it is at the present time relatively inconsequential in the boulder track analysis. On this basis, therefore, the boulder track locations should be representative of lunar soil in general.

This inference is, however, preliminary and would not apply for unusual conditions. It appears that superimposed on both maria and upland areas in many places are materials possibly differing in density. This refers to both solid rock and soil or rock fragments and would include extrusive volcanic materials with high porosity such as scoria and pumice. Lunar ray materials, some of which extend several hundred kilometers from their crater of origin and in places cover much of the surface, may also differ in density. The influence of such variations in density will be considered next.

B. Sensitivity of Results to Variations in Soil Parameters

1. Density: The influence of variations in densities of rock and soil can be appreciated by considering Equation (1-13), which gives the bearing capacity term (left side term) of Equation (1-10). The

bearing capacity term, $q_m/w\gamma_e$, is directly proportional to the density ratio, γ_r/γ, and inversely proportional to the w/D ratio cubed. Since the only density that appears on the right hand side of Equation (1-10) is in the cohesion-term which is only about 3% of the N_γ-term, it follows that variations in density have a major influence only when the ratio of rock density to soil density is changed.

Without the action of atmosphere and running water, it is fairly certain that most lunar soils accumulate in-place. It then follows that the specific gravity of most boulders and the soil particles over which they rolled should be similar. One would therefore expect the density ratio to be fairly constant provided the void ratio or the state of compaction of the material remains the same. There may be, however, notable exceptions such as the case of a dense basalt-like boulder rolling on a loose or high porosity volcanic ash or lunar ray material. Or the case of a light scoriaceous rock rolling on a dense soil. To account for such possible variations, Equation (1-13) was solved for various density ratios in accordance with values listed in Table 1-5. It is to be noted that other combinations of densities could also result in the same density ratios; the values selected merely represent some likely and unlikely situations.

The solution of Equation (1-13) using the density ratios from Table 1-5 is presented in graph form on Figure 1-16. This graph provides a convenient solution of the weight over area expression and shows the significance of the density ratio and the w/D ratio. Within the range of possible values of the density ratio it is apparent that the $q_m/w\gamma_e$ term could triple. This magnitude of change of the $q_m/w\gamma_e$ term would

lead to a ±5-degree difference in the friction angle as determined from Figure 1-18. Hence, using incorrect values of the density ratio could lead to a considerable error in the computed friction angle.

TABLE 1-5

Description					
Rock type	γ_r	Soil type	γ	$\frac{\gamma_r}{\gamma}$	Likelihood of ratio occurrence
Basaltic, vesicular	2.7	Mixed and maria soil	1.6	1.7	Probably common
Basaltic, average porosity (Surveyor results)	3.1	Mixed and maria soil (Surveyor results)	1.5	2.0	Probably common
Porous volcanic rock	1.8	Relatively dense basaltic soil	1.8	1	Possible
Basaltic, average porosity	3.1	Volcanic ash or porous material	1.1	3	Possible
Extra dense volcanic or meteoritic rock	4.2	Light volcanic ash or porous material*	0.7	6	Probably rare
Pumice-like rock	0.7*	Dense basaltic soil	2.3	0.3	Probably very rare

* Bendix Corporation 1968

2. Cohesion: The significance of cohesion depends on the relative magnitude of the coefficient of N_c, 1.1 $\frac{c}{\gamma_e w}$, with respect to the coefficient of N_γ, 0.0314, in Equation (1-10). For all boulders analyzed the $c/\gamma_e w$ term was less than 0.002, with an approximate average value of 0.001. This is only about 3% of 0.0314, and consequently the cohesion term for the boulders analyzed gave an insignificant contribution to the total bearing capacity.

For the more general case, considerably higher values of cohesion could be significant. This possibility will be investigated using the average ϕ of the boulders analyzed, i.e., 34° and $c = 10^3$ dynes/cm^2 as a basis. For $(z/w)_{ave} = 0.234$ and a friction angle of 34°, Figure 1-18 gives a value of 1.15 for $q_m/w\gamma_e$. We may now enter Figures 1-8 to 1-15 with this value $q_m/w\gamma_e$. If we assume $\alpha_{ave} \cong 15°$, we have the following values of ϕ for a 10- and 100-fold increase in cohesion:

Cohesion c	Resulting friction angle ϕ
10^3 dynes/cm^2	34°
10^4 dynes/cm^2	32°
10^5 dynes/cm^2	16°

A cohesion of 10^5 dynes/cm^2 is close to the maximum that has been estimated for lunar soils. A cohesion of 10^4 dynes/cm^2 is somewhat more than the maximum estimated for the Surveyor landing areas. For cohesion greater than 10^4 dynes/cm^2 an incorrect assumption of cohesion could be significant. However, for cohesion less than 10^4 dynes/cm^2, which is the case for the low values believed to exist in lunar soils, an incorrect assumption as to cohesion would have only a small effect on the results.

C. Sensitivity of Results to Measurements

Since the function plotted on Figure 1-16 is inversely proportional to the w/D ratio cubed, small changes in the w/D ratio would be expected to have a large influence on the $q_m/w\gamma_e$ ratio and perhaps the friction angle. To see how serious errors or inconsistencies in measuring the boulder and track dimensions might be, the measurements were made on two different scale photographs as previously described. The difference in the two measurements were computed as follows:

For the diameter

$$\Delta D = \left[1 - \frac{D_{smaller}}{D_{larger}}\right] \times 100$$

For the track width

$$\Delta w = \left[1 - \frac{w_{smaller}}{w_{larger}}\right] \times 100$$

Similarily, the difference in the w/D ratio was computed by

$$\Delta \left(\frac{w}{D}\right) = \left[1 - \frac{(w/D)_{smaller}}{(w/D)_{larger}}\right] \times 100$$

The results of the comparison and the resulting change in the friction angle, $\Delta\phi$, are shown in Table 1-6. The basis for this comparison is $(w/D)_{ave} = .69$ as determined from Figure 1-19 for $\phi_{ave} = 34°$.

Table 1-6

Sensitivity of Results to Measurements

Comparison	ΔD (%)	Δw (%)	Δ W/D (%)	$\Delta\phi$ (°)
Average	9	12	9.6	2
Maximum	32	28	22	5

As shown in Table 1-6 above, the average difference in ϕ for the two measurements would be about 2 degrees. If it can be assumed that the friction angle resulting from averaging the measurements, as was done for the results presented, is closer to the correct value than the result of either of the measurements independently, the friction angles presented in Table 1-4 and on Figures 1-18 to 1-22 may be regarded as including a one degree average error and about 3 degree maximum error due to inconsistencies in measurements. This is quite good considering the scale of the photographs; as better photographs become available, it should be possible to considerably reduce measurement inaccuracies.

It is also to be noted that the change in w/D is likely to be less than the change in either w or D separately as shown in Table 1-6. This is fortunate since the theory shows that the results depend primarily on the w/D ratio.

D. Sensitivity of Results to the Slope Angle

The influence of changes in the slope angle, α, on the resulting friction angle is presented below. Again the average friction angle of 34° was assumed to be for $\alpha = 15°$, and other assumptions are the same as previously used in this discussion.

Slope angle, α	Friction angle, ϕ
0°	30.8°
5°	32.0°
10°	33.3°
15°	34.7°
20°	36.3°
25°	38.0°
30°	40.0°
35°	42.0°

Since slope angles cannot be very accurately determined at this time, the results of ϕ presented in Table 1-3 should be considered to have a probable error of $\pm$ 1° due to incorrect estimation of the slope angle. This would correspond approximately to a $\pm$ 5° difference in the slope angle as shown above.

E. The Theory

Perhaps the biggest shortcomings of the boulder track analysis at the present time are deficiencies in the theory. It is recognized that the failure mechanism assumed or adopted from bearing capacity theory may be unrealistic and that the problem, although clearly dynamic, has been considered static. Our immediate future efforts will, therefore, be directed primarily toward a study of the mechanism of rolling sphere-soil interaction, and toward the development of a better theory.

It is impossible to say how much the values of ϕ may be in error due to limitations of the theory. It is believed, however, that a correct theory would not have appreciably reduced the spread of the results; this is related to a fact measured on the photographs - the w/D ratio. It is likely that a correct theory would shift the entire curves on Figure 1-22 horizontally one way or the other.

F. Summary

The discussion has considered possible effects of incorrect assumptions as to soil parameters, incorrect measurements, incorrect estimates of the slope angle, and inadequacies of the theory. The tangible effects are summarized below:

Cause:	Effect on ϕ:
Incorrect assumption of c (Surveyor range, 10^2 to 10^4 dynes/cm^2)	$\pm$ 2°
Incorrect value of density ratio (range γ_r/γ = 1 to 3)	$\pm$ 5°
Incorrect value of w/D ratio (measurements)	$\pm$ 1 or 2°
Incorrect slope angle ($\pm$ 5°)	$\pm$ 1 or 2°

Of the causes listed above, incorrect estimates of the density ratio have clearly the largest effect on the results. We are therefore left with the following possibilities for the results of ϕ being what they are:

1. The density ratios varied considerably for the boulder tracks analyzed; possibly the state of compaction or the specific gravities varied.
2. The cohesion for some of the locations was more than 10^4 dynes/cm^2.
3. The results reflect the theory used and its limitations.
4. The friction angle varied for the locations analyzed.

Finally, some comment on the potential usefulness of the type of plots presented in Figures 1-18 and 1-19 is in order. In both plots a fairly well defined single curve is implied although the data represent analyses for different slope angles, α, between 0 and 30 degrees as shown on Figures 1-20 and 1-21. Hence, these curves could be used for a rough estimate of the friction angle and bearing capacity of lunar soils from boulder-track measurements.

Even without knowing the slope angle, the resulting friction angle would in the extreme case be possibly 5 degrees in error but usually only 1 to 3 degrees from the correct value based on this theory. It therefore appears that if a better theory could be developed similar graphs could be prepared and fairly reliable values of the actual friction angle of lunar soils could be easily determined from the boulder-track relationship.

Dr. H. Moore of the U.S. Geological Survey, Menlo Park, California, is also performing similar studies, and his results indicate friction angles somewhat lower than our results. It is to be noted that in his analysis the bearing capacity required at the point where the boulder rests is computed, utilizing a full circular bearing area corrected for determinable flatness of boulder shape. In our analysis an attempt has been made to relate the boulder to the track at failure or at the time it was formed and, hence, to determine a limiting friction angle required for stability. Dr. Moore's analysis on the other hand, with the full circular bearing area, determines a friction angle for partially mobilized resistance. Therefore, his values for ϕ are somewhat lower than those obtained here.

VII. CONCLUSIONS AND RECOMMENDATIONS

Lunar boulder tracks from 19 different locations on the moon were utilized to study lunar soil properties. The 69 boulder tracks analyzed are believed to be a sufficient number to form a preliminary basis for certain inferences or conclusions.

1. Boulder track analysis appears to be a promising remote reconnaissance technique for study of soil conditions.
2. Lunar soil and rock properties (cohesion, density, and friction angle) are possibly more variable than anticipated from previous investigations.
3. For the conditions assumed, most of the results centered around a friction angle of 34 degrees. The results of ϕ ranged from 20 to 47 degrees with the majority being between 27 and 41 degrees.

It is recommended that the boulder track analysis be further studied to refine the method and to accumulate more data on lunar surface materials. Proposed work for the near future will concentrate on developing a better theory based on a more realistic failure mechanism for the rolling sphere-slope interaction problem. It is planned to investigate the actual failure mechanism involved in the formation of a track by a rolling boulder. A rational solution to this problem will be valuable not only because of its relevance to the analysis of lunar boulder tracks, but also because of the insight it may provide into soil-wheel interaction, a problem of great importance in connection with lunar roving vehicles.

An opportunity for conducting significant experiments has become available using the facilities at the U.S. Army Engineer Waterways Experiment Station, Vicksburg, Mississippi. During the next few months the WES will be conducting wheel-soil interaction studies using wheels and loading conditions similar to those proposed for lunar roving vehicles. Studies of wheel performance on slopes are to be a major part of this study. The facilities used for these tests will be made available for experimentation involving the rolling of spheres down slopes. It is hoped that information obtained from such experiments may provide sufficient insight into the mechanism of track formation to enable development of a suitable theory.

Contact has been maintained with Dr. H. J. Moore of the Branch of Astrogeology, U.S. Geological Survey, Menlo Park, throughout the conduct of the boulder track studies. His assistance in providing Lunar Orbiter photographs and supporting data, as well as helpful discussion on the methods of analysis and interpretation, is acknowledged with appreciation.

REFERENCES

1. Bendix Corporation, "Summary Report, Lunar Module (LM) Soil Mechanics Study," AM-68-4, November, 1968.

2. Boeing, "Lunar Orbiter Photo Support Data," Orbiters II, III, and V, NASA.

3. Boeing, "Improved Photo Support Data," Orbiters II, III, and V, NASA, February, 1969.

4. Eggleston, J. M., Patteson, A. W., Throop, J. E., Arant, W. H. and Spooner, D. L., "Lunar Rolling Stones," Photographic Engineering, Vol. 34, No. 3, March 1968.

5. Filice, A. L., "Lunar Surface Strength Estimates from Orbiter II Photographs," Science, Vol. 156, p. 1486, 1967.

6. Hackman, R. J., "Generalized Photogeologic Map of the Moon," USGS MAP I-351, Sheet 1 of 4, 1961.

7. Hansen, J. B., "Foundations of Structures - (a) General Subjects and Goundations other than Piled Foundations," Proc. of the Fourth Int. Conf. on Soil Mech. & Found. Eng., London, 1957.

8. J. P. L., Cal. Inst. of Tech., "Lunar Traverse Seminar," Document 760-27, July 1968.

9. Leonards, G. A., "Foundation Engineering," McGraw-Hill Book Co., Inc., 1962.

10. Lunar Orbiter Photo Data Screening Group, Langley Research Center, Langley Station, Hampton, Virginia, "A Preliminary Geologic Evaluation of Areas Photographed by Lunar Orbiter V Including an Apollo Landing Analysis of one of the Areas," NASA, Langley Working Paper (LWP) - 506, February, 1968.

11. Lundgren, H. and Hansen, J. B., "Geoteknik," Teknisk Forlag, Kobenhavn, 1958.

12. Meyerhof, G. G., "The Ultimate Bearing Capacity of Foundations," Geotechnique, Vol. II, 1951, p. 301.

13. Mitchell, J. K. et al., "Material Studies Related to Lunar Surface Exploration," Final Report, Contract NSR 05-003-189, Vol. I, University of California, Berkeley, March, 1969.

14. Moore, H. and Martin, G., "Lunar Boulder Tracks," Orbiter Supporting Data, No. 1, 1967.

15. Nordmeyer, E. F. and Mason, C. C., "Lunar Surface Mechanical Properties Derived from Track Left by Nine Meter Boulder," NASA, NSC Internal Note No. 67-TH-1, February, 1967.

16. Roggeveen, J. J. and Goodman, R. E., "Lunar Surface Length Measurements from Orbiter Photographs," University of California, Berkeley, 1968.

17. Skempton, A. W., (1951): The Bearing Capacity of Clays, Proc. Bldg. Res. Congr., London 1951.

18. The Surveyor Investigator Teams, Scientific Evaluation Advisory Team, and Working Groups, "Surveyor VII Mission Report, Part II. Science Results," J. P. L., Cal. Inst. of Tech., Technical Report 32-1264, 1968.

USGS, Geologic Quadrangle Maps of the Moon:

1. Eggleton, R. E., "Geologic Map of the Riphaeus Mountains Region of the Moon," USGS MAP I-458, 1965.

2. Hackman, R. J., "Geologic Map of the Montes Apenninus Region of the Moon," USGS MAP I-463, 1966.

3. Howard, D. A., and Masursky, H., "Geologic Map of the Ptolemaeus Quadrangle of the Moon," USGS MAP I-566, 1968.

4. McCauley, John F., "Geologic Map of the Herelius Region of the Moon," USGS MAP I-491, 1967.

5. Marshall, C. H., "Geologic Map and Sections of the Letronne Region of the Moon," USGS MAP I-385, 1963.

6. Moore, H. J., "Geologic Map of the Aristarchus Region of the Moon," USGS MAP I-465, 1965.

7. Morris, E. C. and Wilhelms, Don E., "Geologic Map of the Julius Caesar Quadrangle of the Moon," USGS MAP I-510, 1967.

8. Schmitt, H. H., Trask, N. J., and Shoemaker, E. M., "Geologic Map of the Copernicus Quadrangle of the Moon," USGS MAP I-515, 1967.

9. Titley, S. R., "Geologic Map of the Mare Humorum Region of the Moon," USGS MAP I-495, 1967.

10. Wilhelms, Don E., "Geologic Map of the Mare Vaporum Quadrangle of the Moon," USGS MAP I-548, 1968.

SYMBOLS

b	width of equivalent rectangle
c	apparent cohesion
D	diameter of boulder or sphere
H	high resolution
L	length of equivalent rectangle
L_{AB}	arc distance between points A and B
N_c, N_γ, N_q	bearing capacity factors
q	unit bearing capacity
q'	surcharge
q_e	unit bearing capacity in earth gravity
q_m	unit bearing capacity in lunar gravity
R	radius of the moon
r	radius of boulder or sphere
s_c, s_γ, s_q	shape factors in the bearing capacity equation
W	boulder weight
w	track width
z	sinkage or track depth
α	slope angle
β	angle defining equivalent free surface on Meyerhof's charts
ΔD	change in boulder diameter
Δw	change in track width
$\Delta\left(\frac{w}{D}\right)$	change in the track width over diameter ratio
$\Delta\phi$	change in ϕ

SYMBOLS (Contd)

γ	unit weight of soil
γ_e	unit weight of soil in earth gravity
γ_r	unit weight of rock
ϕ	apparent angle of internal friction
θ	angle defining soil-boulder contact
II	orbiter two
III	Orbiter three
VI	Orbiter five

CHAPTER 2

DEDUCTION OF LUNAR SURFACE MATERIAL STRENGTH PARAMETERS FROM LUNAR SLOPE FAILURES CAUSED BY IMPACT EVENTS -- FEASIBILITY STUDY

(T. S. Vinson and J. K. Mitchell)

I. INTRODUCTION

It is generally recognized that terrestrial slope failures may result from (1) loss of soil strength, (2) changes in hydrostatic or hydrodynamic forces, (3) static load changes, and (4) dynamic, e.g., earthquake, loadings. In addition, creep may account for significant downslope movements of material.

While Lunar Orbiter photographs provide evidence of slope failures on the moon, the triggering mechanisms are not yet clear. The extent, if any, to which lunar soils may lose strength with time is not known. Weathering effects are probably minor. While surface temperature variations are large between lunar night and day, the apparently low thermal conductivity of lunar soils means that little effect of temperature variations should be felt at the depths involved in large slope failures.

Since there is no evidence of water in the lunar environment, it is not likely that failures due to (2) above are of importance. Processes leading to large static load changes have not yet been suggested, except as they may result from dynamic events. For example, a cratering event leaves an unsupported crater wall subjected to shear stresses that did

not exist prior to removal of the adjacent material. Failures in crater walls have been observed. Whether or not they resulted from changes in static loading, were developed during formation of the crater itself, or occurred as a result of some later dynamic event is not known with certainty.* Martin (1968) has studied the stability of such slopes using a conventional slices method and assumed seismic coefficients.

A study has been made of the extent to which dynamic loadings might account for lunar slope failures and of the feasibility of estimation of lunar surface material strength parameters from observed slope failures. Three sources of significant dynamic loadings on the moon are (1) seismic events, (2) effects resulting from volcanic activity, and (3) impact cratering events. Little is presently known about seismic or volcanic activity on the moon. Attention has been directed therefore to analysis of ground accelerations that might be generated by impact events and their influence on nearby slopes. Development of crater wall failures during the formation of the crater is not considered herein.

II. METHODS FOR DETERMINING UPPER AND LOWER BOUNDS OF LUNAR SURFACE MATERIAL STRENGTH PARAMETERS USING DYNAMIC SLOPE STABILITY ANALYSES

Dynamic slope stability analyses in the terrestrial environment are generally made in one of two ways: (1) by utilizing a constant acceleration, or (2) by utilizing a variable acceleration. One specific

---

*Hypervelocity impact studies by Oberbeck and Quaide (1967) indicate rather conclusively that the concentric ring geometry observed in many craters probably formed during the impact forming the crater itself.

method from each category might prove useful for analyzing lunar slope failures. The finite element method (Zienkiewicz and Cheung, 1967) allows the stresses at specific points in the slope to be calculated for a given acceleration record. For a failed slope the maximum stresses calculated using the method would represent an upper bound on the strength. For an unfailed slope they would represent a lower bound. This method requires, in addition to the acceleration record, a knowledge of the elastic properties and density of the soil mass and a geometric description of the unfailed slope. Because the elastic properties of lunar materials are at present largely unknown, the finite element method cannot be readily applied to the present problem.

A method has been developed for cohesionless materials (or those exhibiting "apparent" cohesion) by Seed and Goodman (1964). Using this approach a "yield acceleration" (i.e., the acceleration at which sliding will begin to develop under dynamic loading) can be calculated. The yield acceleration for any "cohesionless" slope is given by

$$k_{yg} = \tan (\phi - \alpha + \phi_{SL})\, g \qquad (2\text{-}1)$$

where ϕ = angle of internal friction of the material; α = initial slope inclination; and ϕ_{SL} = a correction factor to account for apparent cohesion and slope end effects.

An upper or lower bound for the friction angle can be calculated depending on whether the slope failed or remained stable if the induced acceleration and the slope angle are known. This is done by substituting

the induced acceleration into Equation (2-1) and solving for ϕ. The usefulness of the result will depend on how closely the field situation approximates the condition of instability, i.e., how close the slope is to a factor of safety of unity.

A recent study for determining the thickness of the fragmental surface layer from observed lunar impact craters has been made by Quaide and Oberbeck (1968). This paper and the method of analysis proposed is limited to slope failures occurring wholly or in part in the fragmental surface layer.

As stated above, the only triggering mechanism for slope failures has been assumed to be shock waves caused by impacting meteorites. The approach used was to: (1) determine the response of a given slope to a given distance from the impact point, (2) to note that if a failed slope can be observed an approximate upper bound for the strength can be calculated; whereas, if the slope is stable, an approximate lower bound for the strength can be calculated. Necessarily, assumptions were needed at almost every stage of the analysis.

III. PREDICTION OF THE RESPONSE OF A SLOPE TO AN IMPACT EVENT

The response of a given slope at a given distance from an impact point must be known in order to calculate strength parameters. Two approaches are possible. Theoretically, the solution to the problem of the response of an elastic medium to an impact event is not possible without a precise knowledge of the energy partition into ground motion

and cratering during impact. Such a calculation involves a knowledge of the equation of state, densities, and certain elastic properties of both meteorite and target materials. Also, the initial mass and velocity of the impacting meteorite must be known.

To the authors' knowledge the solution to the problem of stress wave propagation and subsequent attenuation has not yet been solved for a non-elastic material. Since terrestrial soils and rock masses invariably do not behave elastically, it is perhaps unreasonable to expect that lunar soils and rocks would behave elastically. Thus, with respect to the assumptions necessary to meet the requirements for partition of energy calculations and the fact that the response at a given point cannot be calculated for a non-elastic material, the problem cannot be approached theoretically.

The second approach is through empirical observations and recordings of ground response for similar terrestrial events with corrections for lunar environmental differences. If the general lunar geology of a specific area can be evaluated, then the ground motion response data from a similar impact event in a similar geologic terrestrial environment could perhaps be used with appropriate corrections for the effects of reduced gravity, lack of atmosphere, etc. Unfortunately, there are little, if any, data available for surrounding media response during a terrestrial impact event. Thus, an alternate approach is necessary that will allow the use of ground motion records for similar terrestrial phenomena.

The end product of a hypervelocity impact of a projectile striking and penetrating a target material is a crater-like feature. Excellent

analytic and descriptive treatments of the phenomenon of impact and consequent crater formation have been made (Gault and Heitowit, 1963; Gault, Quaide and Oberbeck, 1966; Nordyke, 1961; Short, 1964). This crater-like feature is remarkably similar to the end product of a high explosive or nuclear explosive cratering event. Impact craters and nuclear explosive craters both have regions (particularly the lower cavity) indicating intense shock overpressures; similar trajectories of ejecta fragments as evidenced by comparable throwout and fallback distributions (for shallow buried explosions) and, of course, similar geometries.

The general mechanism of energy release in each respective event is quite different, however. In the impact event shock waves associated with energy release radiate from a line source, namely, the line of impact. For the nuclear cratering event shock waves radiate from a point source, specifically the point at which the nuclear device is buried. However, at one specific time in an impact event a relative maximum of energy release to the surrounding medium occurs. This release of maximum energy at a certain depth of meteorite penetration can be considered analogous to the point source explosive event. In other words, along the line of impact of a meteorite a maximum energy release occurs at a specific point, just as a maximum energy release occurs at a specific point (the point of burial) in a nuclear cratering event.

Within the framework of these comments and noting that no other alternatives are available, an analytical comparison between the two events must be made if the response prediction at a given point is to

be attempted. This is because response data and prediction procedures are available for explosive events (not necessarily cratering events); whereas they are not for impact events.

Short (1964) and Gault, et al. (1966) caution against the interpretation and application of explosive cratering data to impact craters. Since the processes of crater formation by nuclear and impact events differ, Short specifically notes that all physical dimensions will not be the same for the same effective depths* of burst and equivalent yields.

For an explosion, apparent crater depth and apparent crater diameter are related to the depth of burial (Figure 2-1). Generally these dimensions are "scaled" meaning simply that a given physical dimension (apparent crater depth, depth of burial, or apparent crater diameter) is divided by the explosive yield to an appropriate power. Effectively then, the dimensions are normalized to a yield of unity in whatever units are used. This aids in comparing the relationship of the physical dimensions to one another, in that data can be used over a wide range of yields if they are scaled. It has been found that as the scaled depth of burial increases the apparent scaled crater depth and apparent scaled crater diameter increase until an optimum scaled depth of burial is reached, i.e., a depth of burial is reached at which the physical dimensions reach a maximum for a given explosive yield. Beyond this scaled depth of burial

---

* An effective depth of burst is that depth at which an explosion of the same magnitude as the maximum energy released during an impact event generates a crater of the same dimensions as produced by the impact.

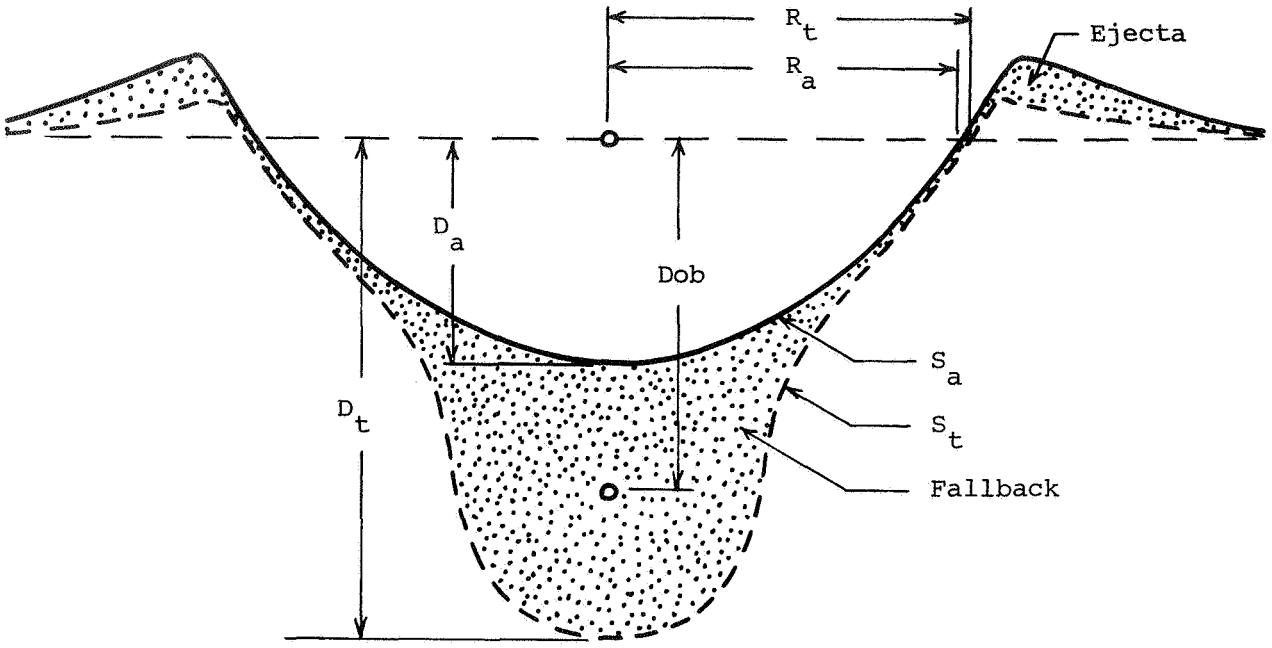

D_a . . . Maximum depth of apparent crater below preshot ground surface measured normal to the preshot ground surface.*

Dob . . Normal depth of burial (measured normal to preshot ground surface).

D_t . . . Maximum depth of true crater below preshot ground surface.

Ejecta . Material above and or beyond the true crater and includes: (1) foldback; (2) breccia — ballastic trajectory; (3) dust — aerosol transport; etc.

Fallback Material fallen inside the true crater and includes: (1) slide blocks; (2) breccia and stratified fallback — ballastic trajectory; (3) dust — aerosol transport; (4) talus; etc.

R_a . . . Radius of apparent crater measured on the preshot ground surface.

R_t . . . Radius of true crater measured on the preshot ground surface.

S_a . . . Apparent crater surface, e.g. rock-air or rubble-air interface.

S_t . . . True crater surface, e.g. rock-air or rock rubble interface.

*All distances, unless specified otherwise, are measured parallel or perpendicular to preshot ground surface.

FIGURE 2-1 CRATER NOMENCLATURE

physical dimensions will decrease. The optimum scaled depth of burial need not be the same for both the depth and the diameter. The relationship of apparent scaled crater radius or apparent scaled crater depth versus scaled depth of burial is consistent for shots fired in similar geologic environments and over a wide range of explosive yields. Thus, what Short implies is that the relationship for the physical dimensions versus scaled depth of burial will not be the same for both impact and explosion cratering.

Most investigators agree that a shallow explosion more closely simulates the impact crater than does a deeply buried explosion. Nordyke (1961) states that "Shoemaker's analysis (1959) suggests that meteor crater corresponds to an explosive-produced crater with scaled depth of burst of about 45 feet." For the purposes of the sample calculation in this report this value of scaled depth is considered initially. The effect of varying this depth of burial is also considered.

Thus, the steps for determining an equivalent yield from which acceleration predictions can be made are: (1) select a physical dimension of an impact crater either apparent radius or apparent depth, (2) calculate an explosive yield by fixing the scaled depth of burial at a specific value and using the relationship between the physical dimension versus scaled depth of burial for an explosive event.

The effects of the lunar environment on cratering must be considered. Tests have been conducted in sand under reduced gravity and reduced atmospheric pressure conditions(Johnson et al,(1968). (To the authors' knowledge they have not been conducted for both conditions acting simultaneously.) The results of these tests showed that with the reduction of either gravity

or atmospheric pressure the apparent physical dimensions increased for a given yield and depth of burial relative to standard terrestrial conditions. The specific conclusions drawn by the investigators (and used in the calculations of this report) were that, if atmospheric and gravity effects could be superimposed, then the apparent diameters of terrestrial and lunar craters would be in the ratio of 1.0 to 1.4. Johnson, et al. (1968) recommend that caution be exercised in applying these results to explosions with energies greatly in excess of 10^{10} ergs (approximately equivalent to 1 lb of TNT). Since the lunar cratering events of interest herein probably involved energies in the megaton range, the use of the 1 to 1.4 scaling may be questionable. There appears to be no alternative procedure available, however, to account for gravity and vacuum effects.

Ground response prediction equations are not readily available for explosive cratering shots. The data available are for surface or fully contained shots. These two events represent extremes in terms of ground motion. For a surface shot the air-induced ground motion (that due to air shock overpressures) greatly exceeds the contribution due to the direct-induced sources (those due to the momentum transfer of energy to or into the medium adjacent to the detonation point). In contrast, a contained event causes motion only through direct-induced effects. In a terrestrial cratering phenomenon we are in fact dealing with a combination of both of these effects. There is direct-induced motion certainly up until break-through, then air-induced and direct-induced are both present. The relative contribution of each of these would depend on the depth of burial. In the following calculations it is reasoned that the ground

motion for a cratering event can be no greater than that from a contained event at a shallow depth of burial. The contained event explosion is assumed to be the same magnitude as that necessary to produce a given crater if the explosive was buried at the shallow depth of burial.

Due to the lack of atmosphere there can be no air-induced effects on the moon. The procedure outlined above is at best a gross approximation to the actual impact cratering event. In the impact event the cavity is vented from the start thus reducing the effect of any direct-induced motion. The actual significance of the reduction in the impact event is unknown.

IV. SAMPLE CALCULATION TO PREDICT LUNAR SURFACE MATERIAL STRENGTH PARAMETERS

In the predictions of lunar slope response it is necessary to select an impact crater feature that developed subsequent to the formation of the slope under investigation. To this end the "fresh" impact crater found in framelets 621 and 622, HR spacecraft frame No. 189 of the Orbiter Mission III photos has been selected (Figure 2-2). It appears clear that this feature developed later than the formation of any of the slopes of the walls of the neighboring craters. For this calculation two extremes are possible with the available empirical scaling relationships and the hypothesized stratigraphy of the lunar surface. The meteorite may be assumed to have penetrated a granular deposit or it may be assumed to have penetrated a massive rock formation. Both possibilities have been considered, although in practice it would only be necessary to decide which extreme best represented in situ conditions.

The first step is to select the physical dimensions to be used in the calculation. The apparent crater diameter was used, since it can be

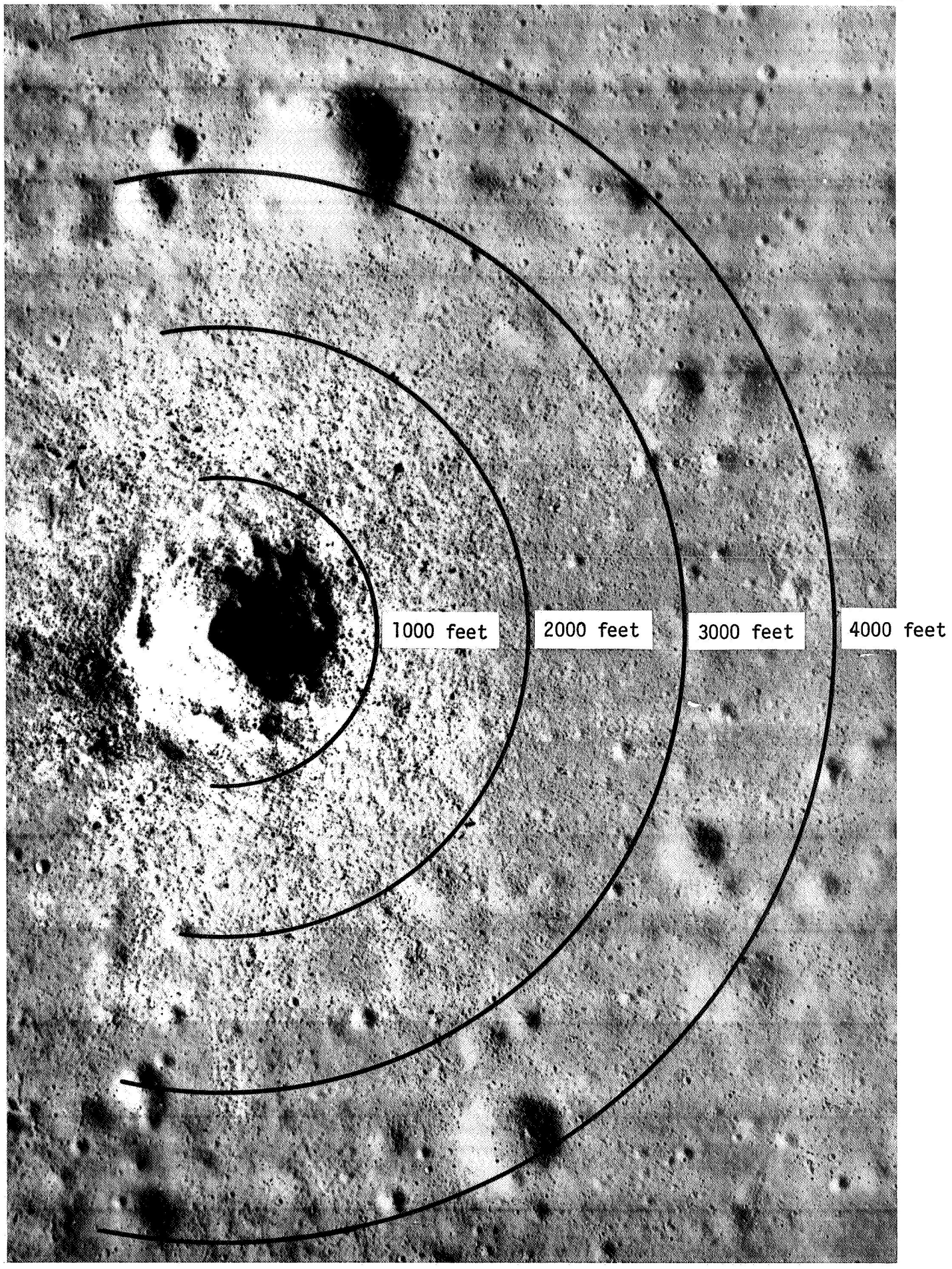

FIGURE 2-2 "FRESH" IMPACT CRATER

scaled directly from the photograph, for all practical purposes, without the additional necessity of working with selenographic coordinates, relative spacecraft position, relative sun angle and position, etc., needed for the calculation of feature heights or depths on the lunar surface. For the impact crater feature in question, the apparent diameter is approximately 400 meters or 1312 feet. Using the scaled radius versus scaled depth of burial relationship suggested by Sauer, et al. (1964) for desert alluvium,

$$R_s = 112.5 + (7.55 \times 10^{-1})Z_s - (9.6 \times 10^{-6})Z_s^3 - (9.11 \times 10^{-12})Z_s^5 \qquad (2\text{-}2)$$

where,

$R_s = \frac{R}{W^{1/3.4}}$, scaled radius

$Z_s = \frac{Z}{W^{1/3.4}}$, scaled depth of burial

R = apparent crater radius, feet

Z = depth of burial, feet

W = explosive yield, kilotons (kT) of TNT.

Then, for example, take Z_s = 45 feet

$$R_s = 112.5 + (7.55 \times 10^{-1})\ 45 - (9.6 \times 10^{-6})\ 45^3 - (9.11 \times 10^{-12})\ 45^5$$

R_s = 145.58 ft

Considering gravity and atmospheric effects

$$\frac{R_{moon}}{R_{earth}} = 1.4$$

$R_{earth} = R_{moon}/1.4 = 656/1.4 = 469$ feet

And from above

$$W^{1/3.4} = R/R_s$$

$$= 469/145.58 = 3.22$$

and $W = 53$ kT,TNT

Table 2-1 shows the variation in yield for different assumptions of scaled depth of burial. In the calculation above, if gravity and atmospheric effects are neglected, a yield of 166 kT, TNT results. If the target medium is basalt then a scaled depth of burial of 45 ft. yields 235 kT TNT. This is calculated with the aid of Figure 2-3, which shows the relationship between scaled crater radius and scaled depth of burial for explosive events in basalt. Note that scaling to the 1/3 power is used. To the authors' knowledge there is no available information to account for the effect of the lunar environment on cratering events in basalt.

The calculation method outlined by the Air Force Systems Command (1967) has been followed for response prediction. It is necessary to assume a seismic velocity of the material, which for desert alluvium can be taken as approximately 5,000 fps and for basalt as approximately 16,000 fps. Distances from the event to slopes where it is desired to know the acceleration are determined. Figure 2-4 shows peak particle acceleration as a function of distance for three materials and an assumed 1-kT event. In order to use this figure it is necessary to use a slant range for the contained event divided by the yield scaled to the 1/3 power. The slant range is the distance from the depth of burial (assumed depth of maximum energy release for an impact event) to the point in question on the lunar surface. If, for example, it is desired to know the response at 3,000 feet for a scaled depth of burial of 45 feet in desert alluvium, one would first convert the scaled depth of burial to a true depth:

$$\text{true depth} = (45 \text{ feet})(53)^{1/3} = 169 \text{ feet.}$$

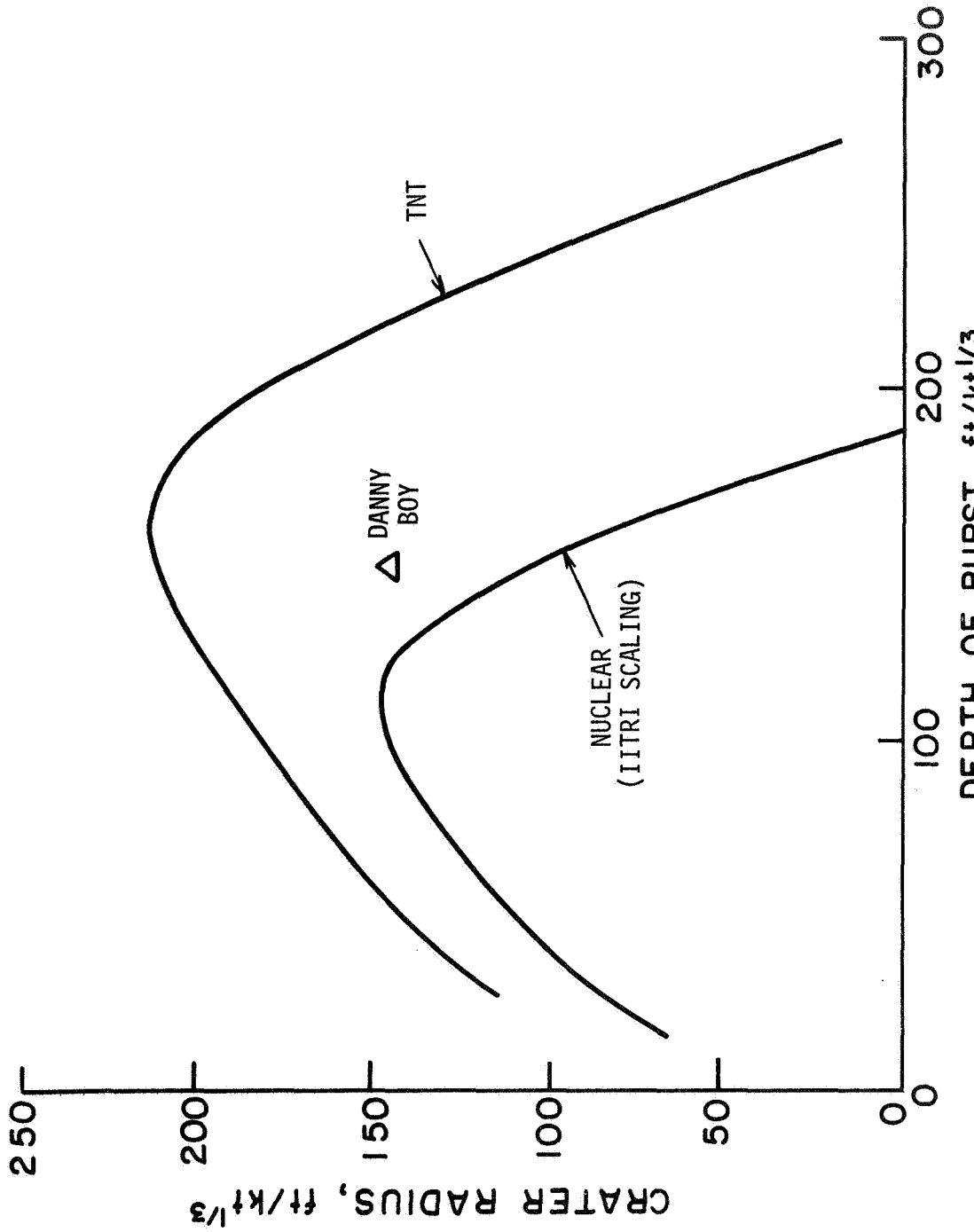

FIGURE 2-3 NUCLEAR AND He CRATER RADIUS VS DOB IN NTS BASALT (After Sauer et al., 1964)

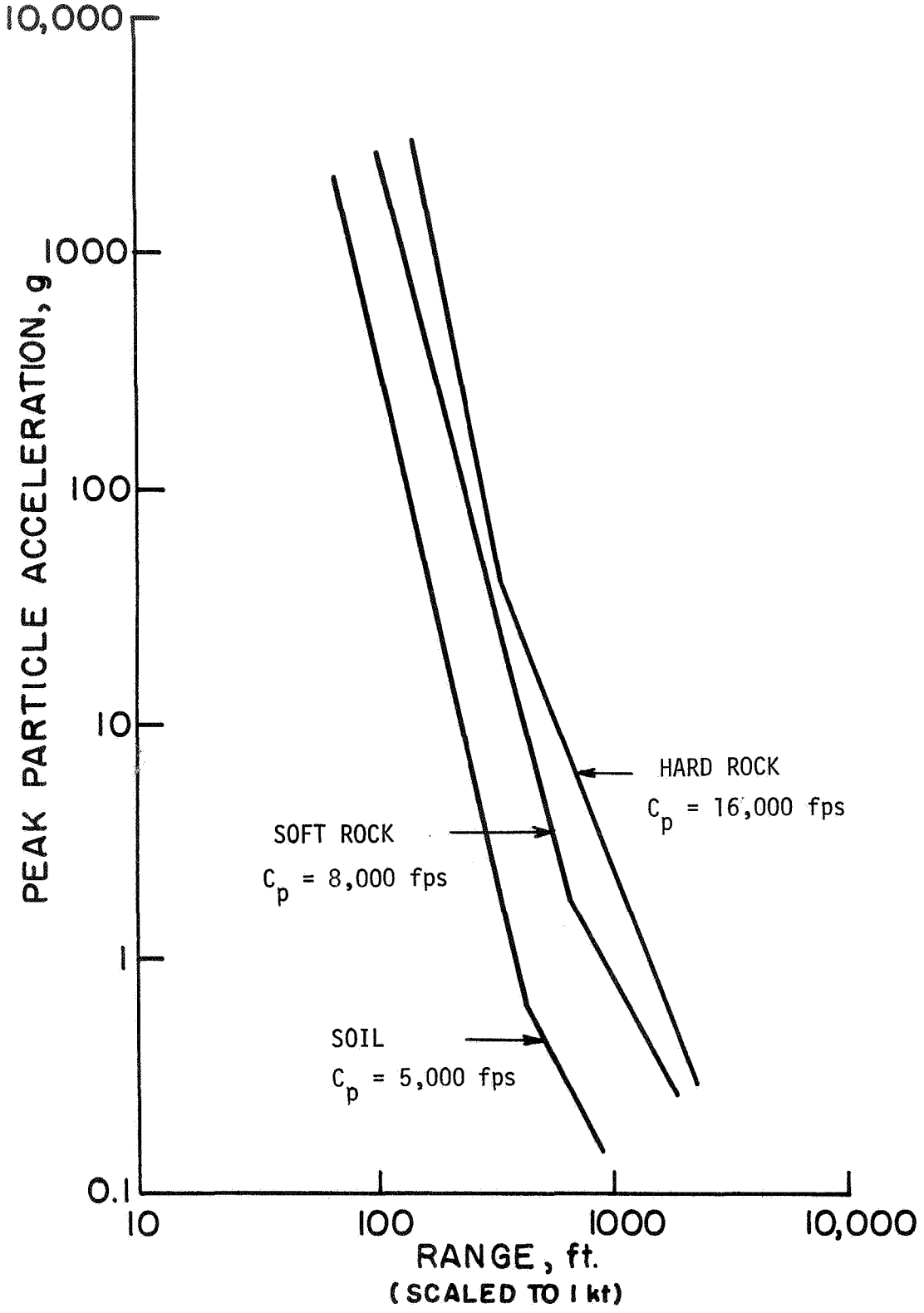

FIGURE 2-4 PEAK RADIAL PARTICLE ACCELERATION SCALED TO 1 kT
(After AFSC, 1967)

TABLE 2-1

Variation in Yield for Different
Assumptions of Scaled Depth of Burial

Yield in kT, TNT

	Terrestrial environment			Corrected for lunar environment		
Scaled depth of burial, ft	30	45	60	30	45	60
Yield (kT-TNT) in Alluvium	70	53	42	217	166	135
Yield (kT-TNT) in Basalt	430	235	170	-	-	-

Then, slant distance = $\sqrt{169^2 + 3002^2}$ = 3005 feet. Scaling to the 1/3 power

$$\text{scaled distance} = \frac{3005}{(53)^{1/3}} = 812 \text{ feet}$$

Entering Figure 2-4 with this value the acceleration is 0.18 g. The complete relationships for alluvium and basalt for a depth of burial of 45 feet are shown in Figure 2-5. Figure 2-5 also shows the relationship assuming the impact was essentially a surface event. Here the procedure is exactly the same as for the contained event but the yield is calculated as

$$W_e = (0.01)(W_n)\ (6.00 - \log_{10} W_n) \quad \text{(from Air Force Systems Command, 1967)} \qquad (2\text{-}3)$$

where, W_n = nominal yield in kT, TNT. The particle acceleration for an event with a seismic velocity different than those shown in Figure 2-4 is proportional to the square of the ratio of the seismic velocities.

V. APPLICATION OF RESULTS

It is next necessary to separate those slopes around the impact crater that have failed from those that may be considered as stable. This is in fact one of the most difficult tasks in the analysis. Rather than attempting this at the present time, which would complete the strength parameter determination as outlined previously, another aspect of the total problem has been considered. The problem of distinguishing failed versus unfailed slopes will be taken up in the concluding remarks.

Best estimates indicate that lunar surface material has an angle of internal friction of approximately 35° to 37° and a cohesion intercept of approximately 0.1 psi. This value of cohesion and a slope length between 20 feet and 50 feet implies an angle ϕ_{SL} equal to approximately 4° (Goodman and Seed, 1966). As a very conservative assumption, relative to the value of yield acceleration for a given material, it will be assumed that $\alpha = 0°$.

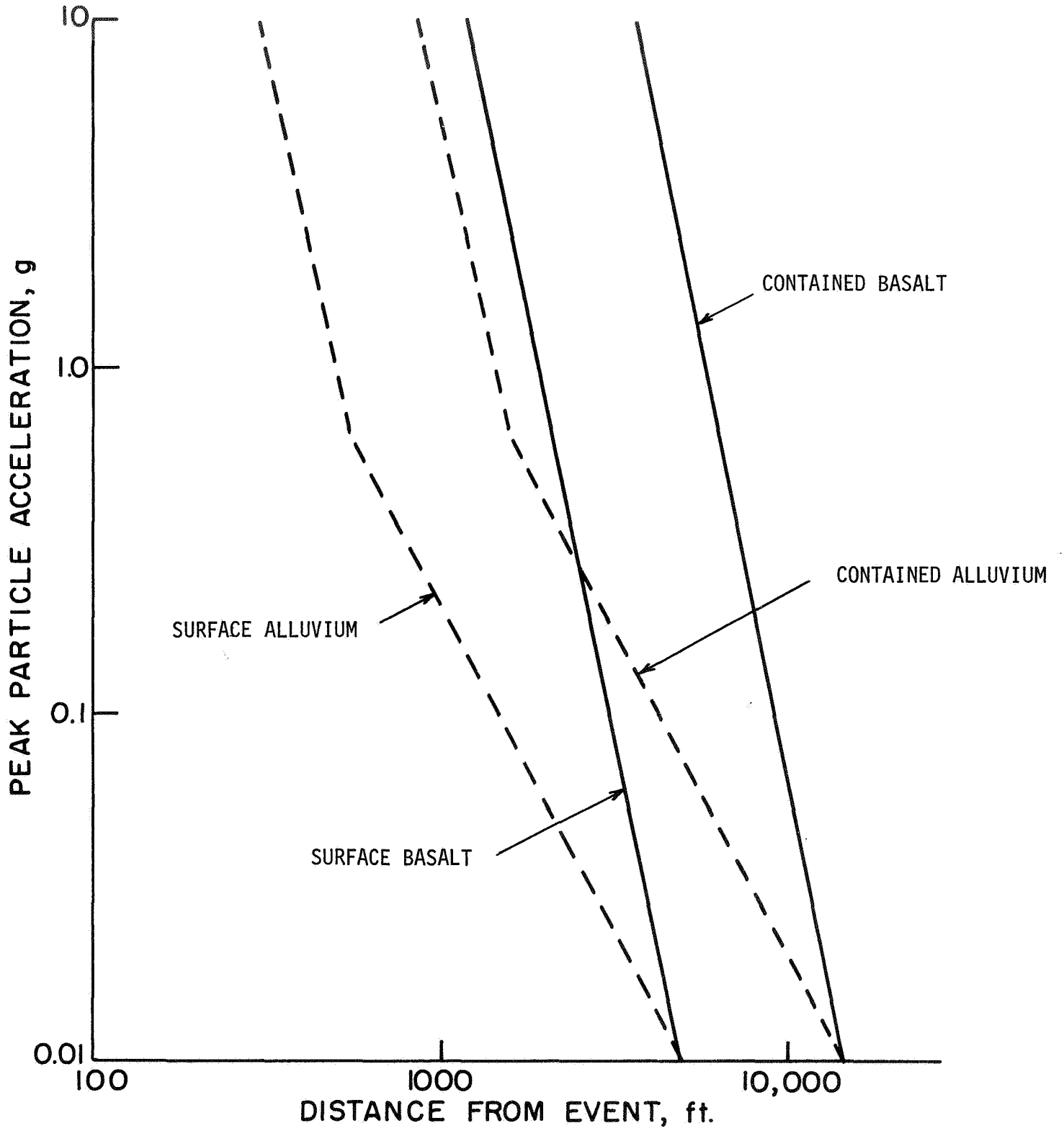

FIGURE 2-5 RESPONSE CURVE FOR IMPACT EVENT IN SAMPLE CALCULATION

This means that the slopes under consideration are flat, which is of course incorrect. As the value of the slope inclination increases the magnitude of the yield acceleration will decrease. Substituting in these values

$$K_{yg} = \tan (37° - 0° + 4°)g$$

$$K_{yg} = 0.87\ g$$

for

$$g_{moon} = 1/6 g_{earth}$$

$$K_{yg} = (0.87)(1/6)g_{earth} = 0.145 g_{earth}$$

This value thus represents an approximate yield acceleration for a flat lunar slope between 20 and 50 feet long. Entering Figure 2-5 with this yield acceleration it is found that any slope at 3500 feet in alluvium or 8400 feet in basalt from the center of the impact crater would be expected to have failed. In fact, there are slopes within this limit that did not fail (see Figure 2-2).

There are at least five factors that could have led to this difference between prediction and observation. These are:

(1) The scaling law relationship used is incorrect.

(2) Wave propagation and particle acceleration in the lunar environment is substantially different than in the terrestrial environment.

(3) The procedure used for prediction of impact cratering effects on the basis of explosive cratering data is incorrect.

(4) The time over which accelerations in excess of the yield acceleration occur is too short to allow failure deformations to take place.

(5) Dynamic soil strengths in the lunar environment are high.

The first three factors relate to response prediction while the last two are concerned with yield acceleration prediction and material properties. Each of these factors may be considered separately.

(1) As noted, the exponent used in the scaling relationship is very important and the consequences of using $W^{1/3}$ as opposed to $W^{1/3.4}$ can be quite significant. Murphey (1959) lends some insight into the problem in his conclusion that in simple cube root scaling no consideration of overburden pressure is made. Chabai (1959) also arrived at the conclusion that $W^{1/3.4}$ should be used rather than $W^{1/3}$ in desert alluvium. For the calculations herein, scaling to the 1/3.4 power was used for the explosive yield associated with the apparent crater radius in alluvium, while scaling to the 1/3 power was used in calculating the yield in basalt and the response data (as suggested in the reference). It would be difficult to assess the variation this source of error might cause, in that the original data from which these empirical prediction curves were derived are not immediately available.

(2) Two general types of waves are of interest in "shock" wave calculations. They are compressional and shear waves. The general formulation for both is given below.

$$C_p \text{ (compressional wave)} = \left(\frac{E(1-\nu)}{\rho(1+\nu)(1-2\nu)}\right)^{1/2} \qquad (2\text{-}4)$$

$$C_s \text{ (shear wave)} = \left(\frac{E}{\rho^2\ (1+\nu)}\right)^{1/2} \qquad (2\text{-}5)$$

where, E = Young's modulus of elasticity; ν = Poisson's ratio; ρ = mass density. For granular materials and moderate stress levels, E can be given by $E = K(\sigma_3')$ where, K = a constant dependent on material characteristics and relative density, n = an exponent dependent on material

type, σ_3' = effective confining pressure. In that σ_3' is directly proportional to the overburden stress and the overburden stress is directly proportional to gravity, in the lunar environment one would expect that for a given depth the value of σ_3' would be one-sixth its value on the earth for similar soil conditions. The exponent n appears to range from about 0.3 to 0.5. Thus $(C_p \text{ or } C_s)_{moon}$ may be of the order of 0.76 to 0.64 $(C_p \text{ or } C_s)_{earth}$ for cohesionless materials. According to elastic theory, particle velocity is inversely related to the wave propagation velocity. Particle acceleration is inversely related to the square of wave progagation velocity. Thus, in the lunar environment, if n = 0.5, $a_{p_{moon}} = a_{p_{earth}} (1/0.64)^2$, $a_{p_{moon}} = (2.44)a_{p_{earth}}$. This obviously means that particle accelerations in the lunar environment should be 2.44 times greater than in the terrestrial environment. If this is true, then for the impact crater in the sample calculation the range within which failure could occur for the calculated yield acceleration would be increased to 6,000 feet. This does not answer "why?" slopes didn't fail, but rather, affirms that perhaps even more slopes should have failed but didn't if the stress waves propagated in surface material.

(3) Figure 2-6 shows the variation of ground accelerations in alluvium with distance for both contained and surface events of several yields. Figure 2-7 shows similar data for events in basalt. Referring back to Figure 2-5, it can be seen if the event in the sample calculation behaved as a surface explosion then slope failures would be expected only for slopes nearer than 1,200 feet in desert alluvium and 2,800 feet in basalt.

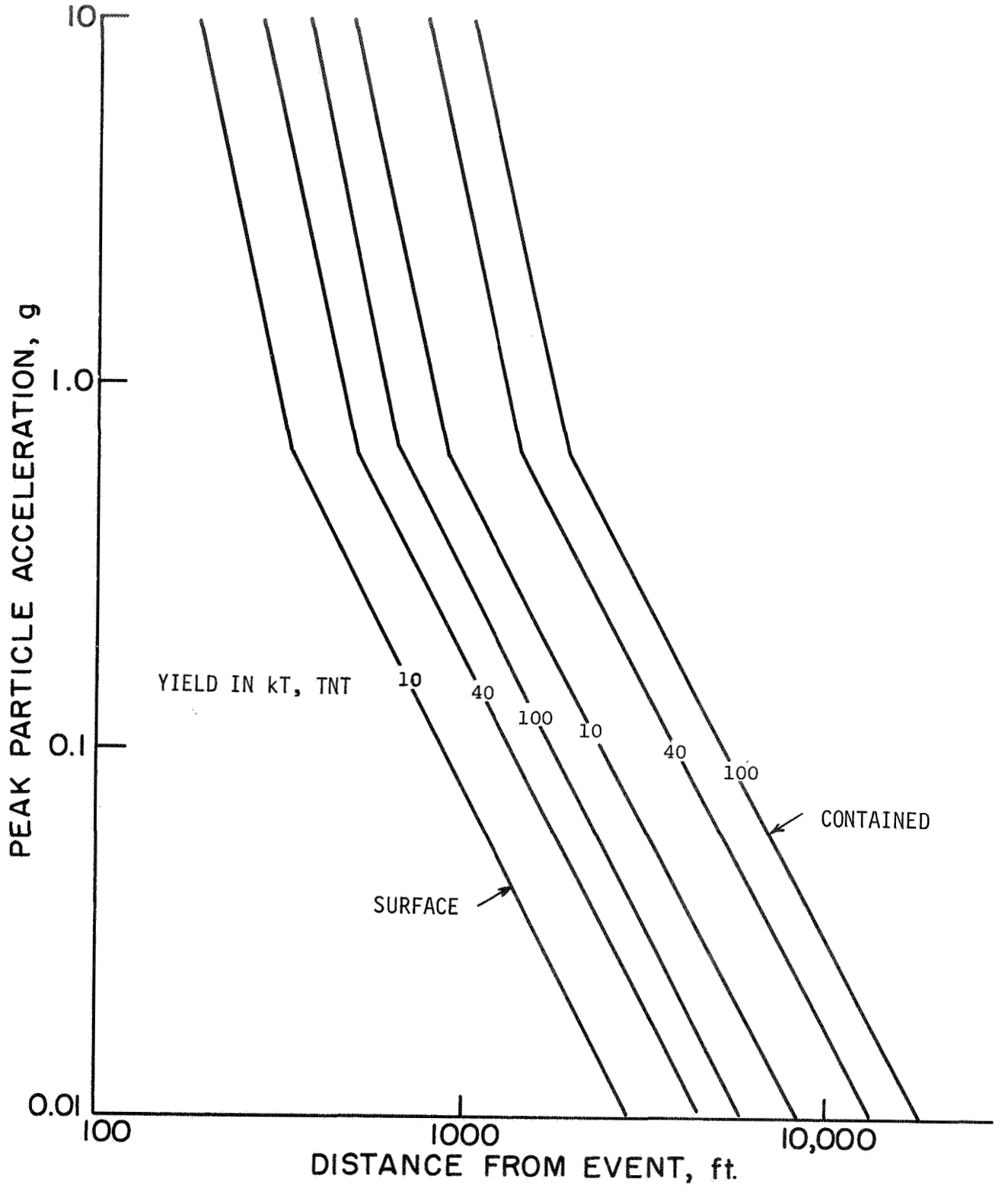

FIGURE 2-6 VARIATION OF RESPONSE CURVES FOR DIFFERENT YIELDS IN ALLUVIUM

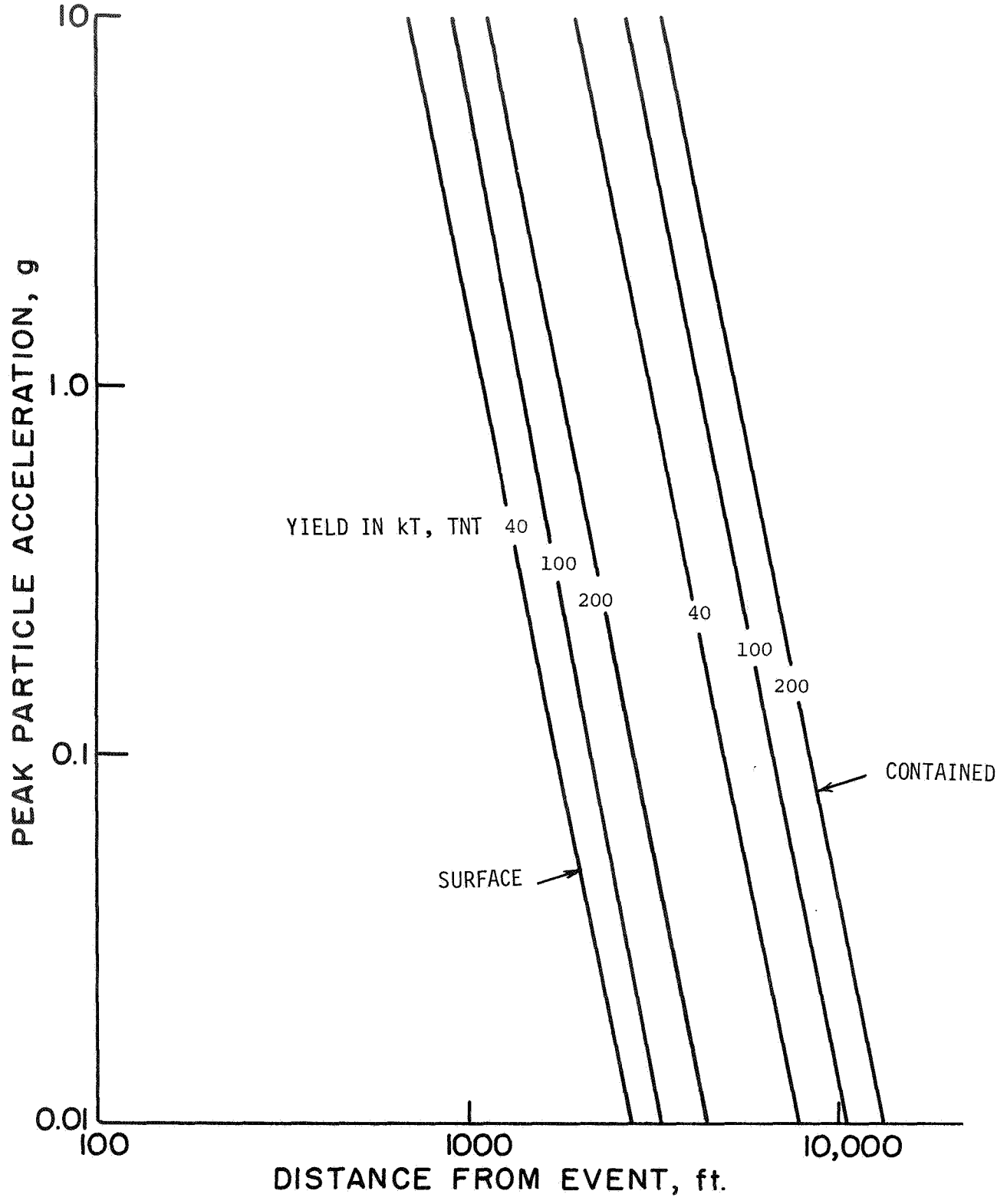

FIGURE 2-7 VARIATION OF RESPONSE CURVES FOR DIFFERENT YIELDS IN BASALT

Furthermore, since the meteorite impact event is essentially a cavity open from the beginning, it is not unreasonable to expect that when the maximum concentration of energy release occurs it would be similar to a surface event.

Relative to the analogy drawn between the impact event and the nuclear explosive, it should be noted that the meteorite is doing work (releasing energy) during the entire period of penetration. Thus, it might not require as much energy to produce a given size crater, in that most of the work of formation had been performed prior to the attainment of maximum energy release. If this were the case for our sample calculation and a 10-kT event in alluvium perhaps better represented the maximum energy release, then slope failures would be expected only within a range of 2,000 feet from the center of the impact crater in Figure 2-2.

(4) Seed and Goodman (1964) mention that "...the magnitude of deformation of a sliding mass under the action of a horizontal acceleration depends not only on the magnitude of the acceleration involved, but also on the time interval for which it is maintained. Thus, an acceleration pulse of short duration may induce a force considerably in excess of the yield acceleration, yet deformations may be negligible because of the short period for which it is mobilized." In addition they conclude that since the yield acceleration was derived independently from the time history of accelerations it would be more reasonable to call the acceleration causing a displacement of one grain diameter the "yield acceleration." Gault, et al. (1966) suggest that during the compression stage of crater development (that stage during which kinetic energy is transferred from the impacting meteorite into the target) shock transient times would vary

from 10^{-3} to 10^{-1} seconds for natural meteorite bodies ranging from 10 meters to 1 km in diameter, respectively. It is only during a fraction of this interval that the maximum energy concentration is reached. Thus the time over which maximum accelerations act may be very small, perhaps a few milliseconds. Whether or not this might represent too short an interval for deformations to occur in a lunar material is, of course, unknown.

(5) From a summary of dynamic test results for dry sands (Schimming et al., 1966) it can be concluded that for "rise times" between approximately 10^{-2} to 10^{-3} seconds the ratio of the maximum dynamic strength to the maximum static strength is usually no greater than 10%. This is in the terrestrial environment. Halajan (1962) studied the effects of gravity on soil strength and concluded that gravity could have a significant influence on the inertial contribution to shearing resistance during dynamic loading. Specifically he developed the following expression for the ratio of the total force to cause failure to the soil strength under static loading conditions:

$$\frac{S_d}{S_c} = \frac{M_s \cdot a + M_n \cdot g \cdot \tan \phi}{M_n \cdot g \cdot \tan \phi} \qquad (2\text{-}6)$$

where, M_s = mass of soil in failure zone; M_n = mass of material normal to failure plane; a = acceleration; g = acceleration due to gravity; ϕ = angle of internal friction; $S_c = M_n \cdot g \cdot \tan \phi$; $S_d = S_c + F$, $F = M_s \cdot a$. When loading times are on the order of 10^{-1} second or less in a reduced gravity field then the inertial term will become significant. This is shown in Figure 2-8 where it can be seen for load dwell times of 10^{-1} the

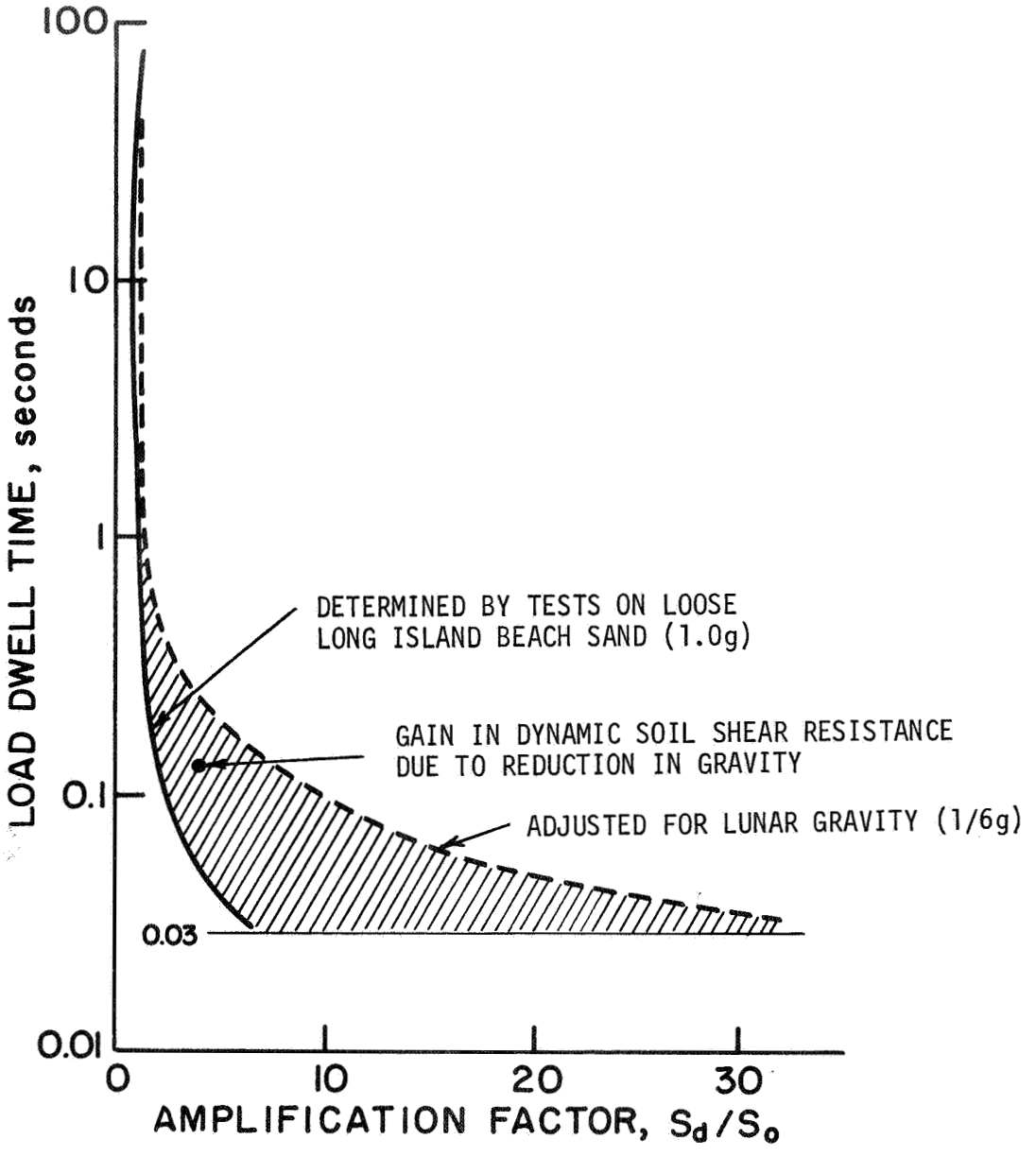

FIGURE 2-8 THE INFLUENCE OF REDUCED GRAVITY ON THE INERTIA CONTRIBUTION TO SHEARING RESISTANCE DURING DYNAMIC LOADING (After Halajian, 1962)

value of equation (2-6) is approximately 10 and for load dwell times of 10^{-2} would be greater than 40 or 50. This may, as most of the past factors, explain in part why lunar slopes might not fail during an impact event.

VI. IDENTIFICATION OF FAILED AND UNFAILED SLOPES

The most difficult task in the total problem, assuming that all other difficulties could be overcome, is to identify a lunar slope failure and to determine whether or not it can be attributed to a specific impact event. Identification of unfailed slopes, with the understanding that sufficiently small surficial deformations may have occurred, presents fewer problems. Basically, if there appear to be no lineations, changes in shadowing, or changes in albedo in a given slope, then the slope most likely has not experienced failure. The converse of these criteria is not necessarily applicable for the identification of failed slopes but they are in fact the most useful indicators. The constant bombardment of small particles on the lunar surface can, with time, mask a slope failure. This is but another aspect of the problem.

In the general formation of craters there are three distinct stages of development. These are in order of occurrence: 1) a compression stage; 2) an excavation stage; 3) a modification stage. During the third stage the principal process is slumping of the peripheral rim structure into the crater basin. This perhaps best accounts for the appearance of fresh craters. It could easily be argued that slope failures identified by several investigators are merely a masking of this type of feature caused by the constant bombardment of small particles.

Presently this, or any other method of analysis involving lunar slope failures, relies on the Orbiter photographs. The best available are the high resolution Orbiter III photographs with a scale of approximately 1:10,000. Orbiter I, II, IV, and V photographs are at a scale of approximately 1:22,000. None of the Orbiter photographs allow positive identification of lunar slope failures. They can provide, with proper judgment, a reasonable assessment of variations in lunar slopes that indicate probable slope failures. There is a dependence on the amount of light on the photograph. Too much or too little will render the photograph useless. The stereo coverage of certain areas is only a little more helpful in the identification of slope failures.

Finally the analysis relies on the determination of the relative time of formation of adjacent craters. To this end it was reasoned that fresh craters occurred later than any of the "softer" visible craters surrounding them. Unfortunately, there is a marked lack of high quality Orbiter photographs showing such events.

VII. CONCLUSIONS AND RECOMMENDATIONS

The potential applicability of calculating lunar surface material strength parameters from dynamic analysis of observed lunar slope failures appears to be severly limited as evidenced by the considerations in the preceding pages. It is concluded, therefore, that analysis of lunar slopes using dynamic considerations and Orbiter photographs is not at the present time a particularly fruitful approach for quantitative determination of lunar soil strength parameters. This does not mean, however, that static analysis based on data acquired during Apollo missions will not be

of value. They will, in fact, be imperative, if the stability of different areas is to be assessed, and hazards related to the operation of roving vehicles and astronauts on slopes are to be estimated.

REFERENCES

1. Air Force Systems Command (1967) Effects of air burst, ground shock, and cratering on hardened structures. AFSCM 500-8, March 1967, USAF.

2. Chabai, A. J. (1959) Crater scaling laws for desert alluvium. SC-4291(RR), December 1959, Sandia Corporation.

3. Gault, D. E., and E. O. Heitowit (1963) The partition of energy for hypervelocity impact craters formed in rocks. Proceedings of the Sixth Symposium on Hypervelocity Impact, Vol. II, Pt. II, 1963, pp. 419-456.

4. Gault, D. E., W. L. Quaide, and V. R. Oberbeck (1966) Impact cratering mechanics and structures. Presented at the Conference on Shock Metamorphism of Natural Materials at Goddard Space Flight Center, Greenbelt, Maryland, April, 1966.

5. Goodman, R. E., and H. B. Seed (1966) Earthquake-induced displacements in sand embankments. Journal of the Soil Mechanics and Foundations Division, ASCE, Vol. 92, No. SM2, Proc. Paper 4736, March 1966.

6. Halajian, J. D. (1962) Vehicle-soil mechanics on the moon. Report No. ADR 04-04-62.2, October 1962, Engineering Department, Advanced Development Program, Grumman Aircraft Engineering Corporation.

7. Johnson, S. W. and J. A. Smith, E. S. Franklin, L. K. Moraski, and D. J. Teal (1968) Gravity and atmospheric pressure scaling equations for small explosion craters in sand. AFIT TR 68-3, March 1968, Department of Mechanics, Air Force Institute of Technology.

8. Martin, G. L. (1968) Bearing capacity of lunar surface materials. Draft copy of report sent in personal communication.

9. Murphey, B. F., and H. R. MacDougall (1959) Crater studies in desert alluvium. SCTM 119-59(t1), May 1959, Sandia Corporation.

10. Nordyke, M. (1961) On cratering. A brief history, analysis and theory of cratering. UCRL-6578, 1961, Lawrence Radiation Laboratory, Livermore, California.

11. Quaide, W. L. and V. R. Oberbeck (1968) Thickness determinations of the lunar surface layer from lunar impact craters. Journal of Geophysical Research, Vol. 73, No. 16, August 15, 1968, pp. 5247-5270.

12. Oberbeck, V. R. and Quaide, W. L. (1967) Estimated thickness of a fragmental surface layer of oceans procellarum, J. Geogphys. Res. 72, 4697-4704.

13. Sauer, F. M., G. B. Clar, and D. C. Anderson (1964) Cratering by nuclear explosives. DASA-1285(IV), Nuclear Geoplosics, Part Four, Empirical Analysis of Ground Motion and Cratering, The Defense Atomic Support Agency, Washington 25, D. C. May 1964.

14. Schimming, B. B., J. J. Haas, and H. C. Saxe (1966) Study of dynamic and static failure envelopes. Journal of the Soil Mechanics and Foundation Division, ASCE, Vol. 92, No. SM2, Proc. Paper 4735, March 1966.

15. Seed, H. B. and R. E. Goodman (1964) Earthquake stability of slopes of cohesionless soils. Journal of the Soil Mechanics and Foundation Division, ASCE, Vol. 90, No. SM6, Proc. Paper 4128, November, 1964.

16. Shoemaker, E. M. (1959) Impact mechanics at meteor crater, Arizona. Open File Report, July 1959, U. S. Geological Survey.

17. Short, N. M. (1964) Nuclear explosion craters, astroblemes, and cryptoexplosion structures. UCRL-7787, March 1964, Lawrence Radiation Laboratory, Livermore, California.

18. Zienkiewicz, O. C., and Y. K. Cheung (1967) The finite element method in structural and continuum mechanics. McGraw-Hill, London, 1967.